An Analytical Model for Spatially Varying Clear-Sky CO_2 Forcing

NADIR JEEVANJEE,[a] JACOB T. SEELEY,[b] DAVID PAYNTER,[a] AND STEPHAN FUEGLISTALER[c]

[a] *NOAA/Geophysical Fluid Dynamics Laboratory, Princeton, New Jersey*
[b] *Harvard University Center for the Environment, Cambridge, Massachusetts*
[c] *Geosciences Department, Princeton University, Princeton, New Jersey*

(Manuscript received 9 October 2019, in final form 20 August 2021)

ABSTRACT: Clear-sky CO_2 forcing is known to vary significantly over the globe, but the state dependence that controls this is not well understood. Here we extend the formalism of Wilson and Gea-Banacloche to obtain a quantitatively accurate analytical model for spatially varying instantaneous CO_2 forcing, which depends only on surface temperature T_s, stratospheric temperature, and column relative humidity (RH). This model shows that CO_2 forcing can be considered a swap of surface emission for stratospheric emission, and thus depends primarily on surface–stratosphere temperature contrast. The strong meridional gradient in CO_2 forcing is thus largely due to the strong meridional gradient in T_s. In the tropics and midlatitudes, however, the presence of H_2O modulates the forcing by replacing surface emission with RH-dependent atmospheric emission. This substantially reduces the forcing in the tropics, introduces forcing variations due to spatially varying RH, and sets an upper limit (with respect to T_s variations) on CO_2 forcing that is reached in the present-day tropics. In addition, we extend our analytical model to the instantaneous tropopause forcing, and find that this forcing depends on T_s *only*, with no dependence on stratospheric temperature. We also analyze the $\tau = 1$ approximation for the emission level and derive an exact formula for the emission level, which yields values closer to $\tau = 1/2$ than to $\tau = 1$.

KEYWORDS: Climate change; Greenhouse gases; Radiative forcing

1. Introduction

Changes in Earth's CO_2 greenhouse effect (i.e., CO_2 radiative forcing) have been a primary driver of past and present climate changes, and are well simulated by state-of-the-art radiation codes (e.g., Mlynczak et al. 2016; Pincus et al. 2015; Oreopoulos et al. 2012; Forster et al. 2011). While this accuracy is critical for credible climate simulation and has thus been a priority for radiation research, less emphasis has been placed on an intuitive understanding of CO_2 forcing and its dependence on atmospheric state variables and hence geography or climate. For instance, zonally averaged clear-sky CO_2 forcing exhibits a marked meridional gradient (e.g., Huang et al. 2016), but what causes this? Answering such questions seems particularly worthwhile given the central role of CO_2 forcing in modern climate change.

While not very well understood, this dependence of CO_2 forcing on atmospheric state (and the ensuing spatial heterogeneity of CO_2 forcing) has been known for some time and has been variously attributed to heterogeneities in surface temperature, lapse rate, water vapor, and cloudiness (Zhang and Huang 2014; Byrne and Goldblatt 2014; Feldl and Roe 2013; Govindasamy and Caldeira 2000; Shine and Forster 1999; Myhre and Stordal 1997; Kiehl and Briegleb 1993). Such studies have typically still emphasized global mean forcing, however, and any attribution of the spatial structure has been only qualitative. Recently, however, Huang et al. (2016, hereafter H16) studied the spatial heterogeneity of CO_2 forcing, and developed a highly accurate multilinear regression model for CO_2 forcing that identified the lapse rate as the most important single predictor for clear-sky CO_2 forcing, followed by water vapor path. While these results point the way toward understanding, such regression models cannot tell us whether their predictors have a fundamental significance or are simply correlated with the state variables that really matter. Furthermore, such models offer limited mechanistic insight beyond that already required to sensibly choose predictors.

Here we attempt to push our understanding further by developing an analytical model based on first principles for spatially varying clear-sky CO_2 forcing. The analytical model builds on that of Wilson and Gea-Banacloche (2012) by accounting for water vapor (H_2O) overlap and nonisothermal stratospheres. It accurately emulates the global distribution of clear-sky radiative forcing produced by benchmark radiation codes, and its simplicity allows us to identify and understand the driving factors behind the geographical distribution of this forcing.

We begin in section 2 with a heuristic derivation of the analytical model, followed by validation against a line-by-line (LBL) benchmark in section 3. In section 4 we use the analytical model to compute the global distribution of CO_2 forcing in the absence of H_2O for a snapshot of GCM output, again comparing to a LBL benchmark. In this CO_2-only case, the analytical model shows that CO_2 forcing arises from surface–stratosphere temperature contrast, and thus that meridional gradients in CO_2 forcing are due almost entirely to the meridional surface temperature gradient. In section 5 we

Denotes content that is immediately available upon publication as open access.

Corresponding author: Nadir Jeevanjee, nadir.jeevanjee@noaa.gov

DOI: 10.1175/JCLI-D-19-0756.1

extend the analytical model to account for H_2O overlap. We again compute global forcing distributions using both the analytical model and the LBL benchmark, and find that H_2O overlap strongly modulates the meridional gradient in CO_2 forcing, by substantially reducing the forcing in the tropics as well as introducing variations from spatially varying column relative humidity. We also find that Simpson's law, which says that H_2O emission temperatures at optically thick wavenumbers do not depend on surface temperature,[1] implies an upper limit (with respect to spatial variations) on CO_2 forcing. Furthermore, this limit appears to be reached in the present-day tropics.

This work focuses primarily on the instantaneous, top-of atmosphere (TOA), clear-sky forcing. While clouds do not qualitatively change the meridional forcing gradient studied here (e.g., Fig. 1c of H16), they do reduce global mean CO_2 forcing by 20%–25% and also modulate its spatial pattern (Pincus et al. 2020; H16), so we consider possible extensions of this work to cloudy skies in the discussion. Our focus on instantaneous TOA forcing also means that we largely neglect the effects of stratospheric temperature adjustment due to increased CO_2 (H16; Hansen et al. 1997; IPCC 1994). This effect is nonnegligible, as the difference between instantaneous TOA forcing and stratosphere-adjusted forcing can be as large as 40% (H16; Zhang and Huang 2014).[2] To address this, in section 7 we extend our formalism to the instantaneous *tropopause* forcing, which better approximates the stratosphere-adjusted forcing, and we argue that our conclusions should apply to stratosphere-adjusted forcing as well. Recent work has identified additional, smaller adjustments to radiative forcing, most notably tropospheric adjustments, but we do not consider these here (see, e.g., Sherwood et al. 2015; Ramaswamy et al. 2019).

2. Theory

In this section we heuristically derive an analytical model for (clear-sky, instantaneous, TOA) CO_2 forcing, where CO_2 is the only radiatively active species (i.e., "CO_2-only") and we consider the 500–850-cm^{-1} spectral region only. This spectral region corresponds to the CO_2 $\nu 2$ bending-vibration mode centered roughly around the 667-cm^{-1} absorption peak, and we will refer to it heuristically as the 667-cm^{-1} band, or simply the CO_2 band.

We begin with a piecewise-exponential parameterization of the spectrum of CO_2 mass absorption coefficients, following the approach of Jeevanjee and Fueglistaler (2020b), Wilson and Gea-Banacloche (2012), and Crisp et al. (1986):

$$\kappa_{\mathrm{ref}}(\nu) = \kappa_0 \exp\left(-\frac{|\nu - \nu_0|}{l}\right). \tag{1}$$

These are reference absorption coefficients evaluated at a fixed pressure and temperature, which we take to be $p_{\mathrm{ref}} = 100$ hPa and $T_{\mathrm{ref}} = 250$ K. Here ν denotes wavenumber (rather than frequency), $\nu_0 = 667.5\,\mathrm{cm}^{-1}$, $\kappa_0 = 50\,\mathrm{m}^2\,\mathrm{kg}^{-1}$ is a representative mass absorption coefficient at ν_0 (discussed further below), and the "spectroscopic decay" parameter $l = 10.2\,\mathrm{cm}^{-1}$ sets the rate at which κ_{ref} declines exponentially away from band center. The parameters l and κ_0 may be obtained by fitting (1) to modeled absorption spectra, but the parameters turn out to depend somewhat on details of the fit (Jeevanjee and Fueglistaler 2020b; Wilson and Gea-Banacloche 2012). Instead, we opt to determine these parameters via optimization as described in section 3.

We now write down the optical depth $\tau_\nu(p)$ at a given wavenumber ν:

$$\tau_\nu(p) = D\kappa_{\mathrm{ref}}(\nu)\int_0^p \frac{q\,p'}{g p_{\mathrm{ref}}}\,dp' = \frac{D\kappa_{\mathrm{ref}}(\nu)q}{2g}\frac{p^2}{p_{\mathrm{ref}}}. \tag{2}$$

Here q is the CO_2 mass concentration (kg kg^{-1}), and $D = 1.5$ is a diffusivity factor required by the two-stream approximation (implicit in what follows), which truncates the 3D radiation field to upwelling and downwelling fluxes (Pierrehumbert 2010; Clough et al. 1992). The factor of p'/p_{ref} in Eq. (2) accounts for pressure broadening, which causes absorption coefficients away from line centers to scale approximately linearly with pressure (Pierrehumbert 2010). We neglect temperature scaling of absorption coefficients.

Although one can use Eq. (2) to solve the radiative transfer equations explicitly, we instead employ the "emission level" approximation wherein we approximate the emission to space from CO_2 at a given wavenumber as occurring entirely at a certain emission level τ_{em}. (The emission level approximation is discussed further in appendix B.) Setting $\tau_\nu = \tau_{\mathrm{em}}$ in (2) and combining with Eq. (1) then yields the "emission pressure" $p_{\mathrm{em}}(\nu, q)$:

$$p_{\mathrm{em}}(\nu, q) = \underbrace{\sqrt{\frac{2\tau_{\mathrm{em}} g p_{\mathrm{ref}}}{Dq\kappa_0}}}_{p_0(q)} \exp\left(-\frac{|\nu - \nu_0|}{2l}\right). \tag{3}$$

The pressure $p_0(q) \equiv p_{\mathrm{em}}(\nu_0, q)$ is an effective emission pressure at the center of the CO_2 band. We show in appendix B that a suitable CO_2 emission level for our purposes is $\tau_{\mathrm{em}}^{CO_2} = 0.5$. With this input, and for $q = 280$ ppmv, we find $p_0 = 16$ hPa, well into the stratosphere.

Equation (3) can also be inverted for the wavenumbers ν_{em} emitting at a given p and q:

$$\nu_{\mathrm{em}}^{\pm}(p, q) = \nu_0 \pm l \ln\left(\frac{Dq\kappa_0 p^2}{2\tau_{\mathrm{em}} g p_{\mathrm{ref}}}\right). \tag{4}$$

Note the logarithmic dependence of ν_{em} on q in this equation.

Figure 1a plots $p_{\mathrm{em}}(\nu)$ from Eq. (3) for an initial CO_2 concentration $q_i = 0.000\,280 \times 44/29 = 0.000\,425$ kg kg^{-1}, and for a final CO_2 concentration of $q_f = 4q_i$. Using a logarithmic axis for $p_{\mathrm{em}}(\nu)$ yields "emission pressure triangles" in the ν–p plane, with the triangle in the q_f case being taller and wider than that from q_i. Crucially, this growth in the triangle means that as q

[1] Simpson (1928), Ingram (2010), Jeevanjee et al. (2021), and references therein.

[2] Consequently, the global mean instantaneous TOA forcing values shown here will be significantly lower than the standard stratosphere-adjusted value of 3.7 W m^{-2} per doubling (Ramaswamy et al. 2001; Myhre et al. 1998).

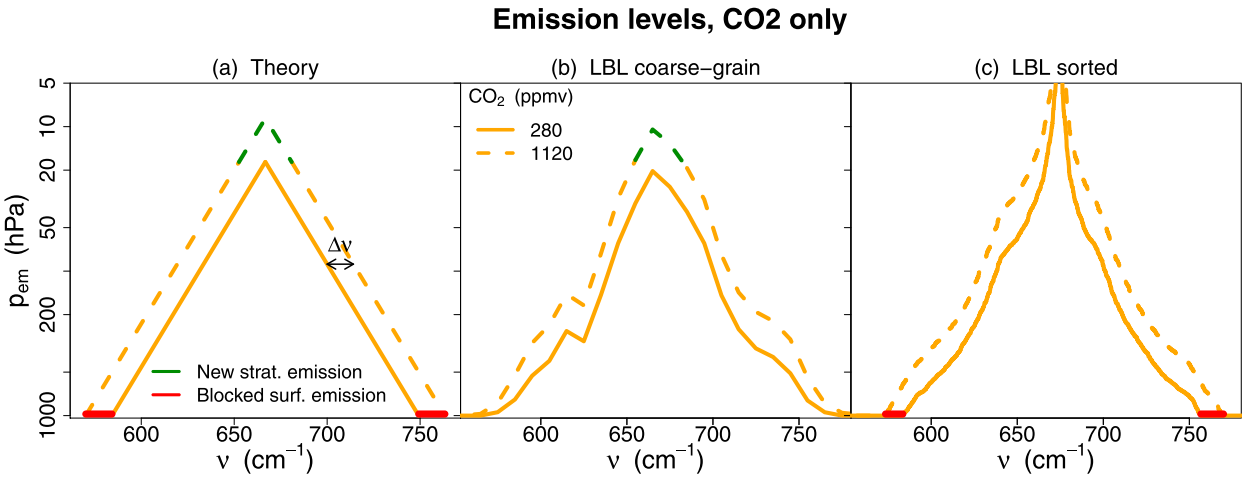

FIG. 1. (a) Graph of CO_2 emission levels as given by Eq. (3) for $q_i = 280$ ppmv and $q_f = 4q_i$. (b) As in (a), but from RFM calculations with CO_2 only for our BASE atmosphere. RFM emission levels are diagnosed by the condition $\tau_\nu = \tau_{em}^{CO_2} = 0.5$, and are geometrically averaged (coarse-grained) over 10 cm^{-1} bins. (c) As in (b), but p_{em} values from the left (right) side of the 667-cm^{-1} peak are separately sorted into descending (ascending) order rather than coarse-grained. The idealized "p_{em} triangles" in (a) roughly match the peak emission pressures in (b) and the blocking of surface emission seen in (c), but do not capture the smallest p_{em} values in (c). The green dashed lines at top in (a) and (b) depict the negative stratospheric contribution to the forcing, the orange lines in all panels depict the null tropospheric contribution to the forcing, and the red solid lines at bottom in (a) and (c) depict the positive surface contribution. Equation (7) quantifies these contributions.

increases, some surface emission is blocked (red line segments) and new stratospheric emission is added (green line segments). In a moment, we will use this insight to write down an analytical expression for CO_2 forcing.

But first, we should validate Eq. (3) and the associated triangle picture in Fig. 1a. To this end, we calculate $p_{em}(\nu)$ with a benchmark line-by-line code (see calculation details in section 3). The line-by-line output has too much fine-scale spectral variation to make a useful comparison to the idealized p_{em} triangles, however, so we must smooth it somehow. This can be done by either coarse-graining (Fig. 1b), or sorting into descending (ascending) order on the left (right) side of the 667-cm^{-1} peak (Fig. 1c).

These panels reveal both strengths and weaknesses of the triangle picture. The peak coarse-grained emission pressures in Fig. 1b quantitatively match those of Fig. 1a, thus confirming the increase in stratospheric emission (green dashed lines). Also, the blocking of surface emission depicted in Fig. 1a is also seen in the sorted output in Fig. 1c (red solid lines; these are not seen in Fig. 1b due to the coarse-graining). At the same time, however, the absorption coefficients and hence emission pressures near the center of the CO_2 band (the Q-branch) exhibit an extreme wavenumber dependence (Coakley and Yang 2014), so that although the coarse-grained p_{em} there is roughly equal to $p_0 = 16$ hPa, the sorted output shows that the most strongly absorbing wavenumbers have p_{em} much less than 16 hPa.[3] Thus while the LBL calculation supports the main features of the triangle picture, the notions of a "representative" peak absorption coefficient κ_0 or an "effective" peak emission pressure p_0 are imperfect idealizations, whose limitations we will encounter below.

We now proceed to a heuristic estimate of the CO_2 forcing $\mathcal{F}$, defined as the difference in outgoing longwave between the q_i and q_f cases. As hinted at above, the key insight is to assess the contributions to the forcing at each *height*, rather than each wavenumber as is customary (e.g., Dufresne et al. 2020). In Fig. 1a, each orange point on the solid q_i curve has a corresponding point on the dashed orange q_f curve at the same height, and thus both points have the same temperature and thus emission to space (neglecting variations in Planck function across these small spectral intervals). The orange segments along the q_i and q_f curves thus make identical contributions to the outgoing longwave, and thus can be neglected in calculating $\mathcal{F}$.[4] There are thus only two contributions to $\mathcal{F}$: the new stratospheric emission from the q_f curve above $p_0(q_i)$ (dashed green), and the blocked surface emission at wavelengths that were previously optically thin (solid red). In other words, the forcing is simply *a swap of surface emission for stratospheric emission*. This new stratospheric emission is of course what cools the stratosphere in response to increased CO_2 (Wang and Huang 2020), and it emanates from a characteristic stratospheric temperature

$$T_{strat} \equiv T\left(\sqrt{p_0(q_i)p_0(q_f)}\right), \tag{5}$$

[3] Indeed, CO_2 is known to emit strongly from not only the stratosphere, but the mesosphere and thermosphere as well (e.g. Curtis and Goody 1956; Mlynczak et al. 2010).

[4] To the extent that the cooling-to-space approximation holds (Jeevanjee and Fueglistaler 2020a), this claim of unchanged cooling-to-space is consistent with a negligible change in tropospheric heating rate for the CO_2-only case, e.g. Fig. 6c of Sejas et al. (2016).

where we take a geometric mean of $p_0(q_i)$ and $p_0(q_f)$. For given surface and stratospheric temperatures T_s and T_{strat}, then, their contributions to the forcing can be estimated once we know the spectral width $\Delta\nu$ over which these contributions are made (Fig. 1a). Using (4), we find that this effective widening of the CO_2 band from changing q_i to q_f is given by

$$\Delta\nu = l \ln\left(\frac{q_f}{q_i}\right). \tag{6}$$

As an aside, we note that the logarithmic dependence of $\Delta\nu$ on q, which follows from (4), arises because $\tau_\nu \sim q e^{-|\nu-\nu_0|/l}$. This implies that for fixed p and $\tau_\nu = \tau_{\mathrm{em}}$, an arithmetic change in ν_{em} (which causes a uniform widening of the CO_2 band) requires a *geometric* increase in q, because the ν dependence of τ_ν is exponential. Since the forcing is proportional to $\Delta\nu$ (Fig. 1a), this is then the origin of the logarithmic scaling of CO_2 forcing [as understood heuristically in, e.g., Pierrehumbert (2010); see also chapter 2 of Seeley (2018)]. Also note that the overall scale of $\Delta\nu$ is governed by the spectroscopic decay parameter l, which also governs the exponential decay of $\kappa_{\mathrm{ref}}(\nu)$ in Eq. (1).[5]

Returning to our derivation, if we denote the hemispherically integrated Planck function by $\pi B(\nu, T)$ (units of W m^{-2} cm^{-1}), and if we approximate the average Planck function across the CO_2 band by evaluating it at ν_0, we can write $\mathcal{F}$ in this CO_2-only case as

$$\mathcal{F} = 2l \ln\left(\frac{q_f}{q_i}\right)[\pi B(\nu_0, T_s) - \pi B(\nu_0, T_{\mathrm{strat}})] \qquad (\mathrm{CO_2\text{-only}}). \tag{7}$$

This expression is equivalent to Eq. (25) of Wilson and Gea-Banacloche (2012). Note that besides the initial and final CO_2 concentrations, the only atmospheric state variables appearing in Eq. (7) are T_s and T_{strat}. This suggests that CO_2 forcing is primarily governed by the surface–stratosphere temperature contrast $T_s - T_{\mathrm{strat}}$, and that the tropospheric lapse rates emphasized by H16 are only a proxy for $T_s - T_{\mathrm{strat}}$, insofar as their vertical integral determines $T_s - T_{\mathrm{strat}}$. Further physical implications of Eq. (7) will be discussed when we study spatial variations of CO_2 forcing in section 4.

3. Line-by-line calculations and parameter optimization

In the remainder of this paper we will test Eq. (7), as well as its extension to account for H_2O overlap, using line-by-line radiative transfer calculations, applied to both idealized single columns and GCM output. This section details those calculations, and uses them to optimize the parameters κ_0 and l appearing in Eqs. (3) and (7), respectively.

a. Line-by-line calculations

Our idealized single column calculations use the Reference Forward Model (Dudhia 2017) for both line-by-line spectroscopy and radiative transfer. We use HITRAN 2016 spectroscopic data for all available spectral lines of H_2O and CO_2 within 500–850 cm^{-1}, for only the most common isotopologue of both gases. We consider highly idealized atmospheric profiles with variable T_s, a constant lapse rate of $\Gamma \equiv -dT/dz = 7$ K km^{-1} up to a tropopause at $T_{\mathrm{tp}} \equiv 200$ K, with constant stratospheric lapse rate Γ_{strat} above. We take relative humidity (RH) to be uniform in the troposphere, while specific humidity is uniform in the stratosphere and equal to the tropopause value. Our baseline CO_2 concentration is $q_i = 280$ ppmv. For many calculations we will use a preferred BASE column with $T_s = 300$ K, tropospheric RH = 0.75, and $\Gamma_{\mathrm{strat}} = 0$. We run RFM at a spectral resolution of 0.1 cm^{-1} (forcing values accurate to within 0.3% relative to benchmark calculations at 10^{-3} cm^{-1}; not shown) and on a vertical grid with uniform spacing of 100 m up to model top at 50 km. Calculations include H_2O continuum effects (unless otherwise noted), which are parameterized using RFM's implementation of the MT_CKD2.5 continuum (Mlawer et al. 2012). CO_2 line shapes include line mixing corrections following Strow et al. (1994). We neglect the 1000-cm^{-1} CO_2 band for the sake of a clean comparison with Eq. (7), but for a quadrupling to 1120 ppmv this band can contribute an additional ~1 W m^{-2} of forcing in a global average, a roughly 10% effect (e.g., Zhao et al. 2018). See Zhong and Haigh (2013) for further analyses of the contributions from additional CO_2 bands, and their effect on the logarithmic scaling of CO_2 forcing.

The "global" LBL calculations (i.e., parallelized calculations on GCM output) shown below follow those of Paynter and Ramaswamy (2012) at a resolution of 0.01 cm^{-1}, using RFM to produce optical depth profiles and then solving the radiative transfer equations with four quadrature points per flux calculation, following the method of Clough et al. (1992). For simplicity the surface emissivity is set to 1 at all locations in all calculations, although the central role we find for surface emission means that uncertainties in surface emissivity (e.g., Feldman et al. 2014) may be relevant for uncertainties in CO_2 forcing.

b. Parameter optimization

We begin with preliminary calculations that we use to set the parameters l and κ_0, and which also serve as a first, idealized test of (7). We start by calculating the instantaneous TOA forcing $\mathcal{F}_{4\times}$ from a quadrupling of CO_2 for our idealized single columns with variable surface temperature T_s, isothermal stratosphere ($\Gamma_{\mathrm{strat}} = 0$), and for CO_2 as the only radiatively active species (CO_2 only). Because these stratospheres are isothermal the parameter κ_0 is not needed to determine T_{strat}, so these calculations can be used to set l without compensating errors from κ_0 optimization.

The results of this calculation, using both RFM as well as (7), are shown in Fig. 2a for various values of l. The value $l = 10.2$ cm^{-1} minimizes the errors in this comparison and yields an excellent fit, and will be used henceforth. Note that this value is close to the $l = 11$–11.5-cm^{-1} range reported in Jeevanjee and Fueglistaler (2020b) and Wilson and Gea-Banacloche (2012) from direct fits to the spectroscopy, and that all values in this range yield a reasonable fit in Fig. 2a.

Next we optimize κ_0. We do this by considering the same columns as in the previous paragraph but with $T_s = 300$ K and

[5] The spectroscopic decay parameter also plays a key role in setting the magnitude of radiative cooling (Jeevanjee and Fueglistaler 2020b).

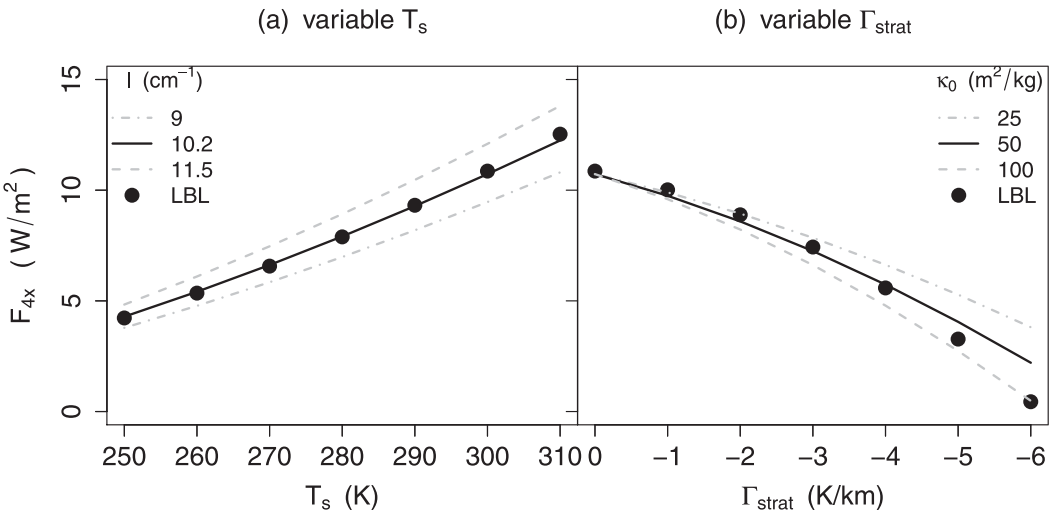

FIG. 2. Comparison of (7) vs RFM for our idealized, CO_2-only single columns with (a) variable T_s and $\Gamma_{strat} = 0$ and (b) $T_s = 300$ K and variable Γ_{strat}. Optimization of l in (a) yields $l = 10.2\,\mathrm{cm}^{-1}$, and optimization of κ_0 in (b) for $-4 < \Gamma_{strat} < 0\,\mathrm{K\,km}^{-1}$ yields $\kappa_0 = 50\,\mathrm{m}^2\,\mathrm{kg}^{-1}$. With these parameter values, the good fit in these panels across a range of T_s and Γ_{strat} provides a first validation of (7).

with variable Γ_{strat}. These more realistic, nonisothermal stratospheres now allow us to probe which κ_0 value yields the most appropriate emission pressure p_0 and hence T_{strat} [cf. Eqs. (3) and (5)]. A comparison of $\mathcal{F}_{4x}$ as computed by RFM and (7) for these columns and for various values of κ_0 is shown in Fig. 2b. This panel shows that for typical values of $-4 < \Gamma_{strat} < 0\,\mathrm{K\,km}^{-1}$, the value $\kappa_0 = 50\,\mathrm{m}^2\,\mathrm{kg}^{-1}$ provides an excellent fit. Note, however, that larger errors appear for larger magnitude Γ_{strat}, showing the limitations of using a single idealized emission pressure p_0 to represent emission near band center; in these extreme cases there are unrealistically warm temperatures near model top (~400 K for $\Gamma_{strat} = -6\,\mathrm{K\,km}^{-1}$) that are probed by only the most absorbent wavenumbers (Fig. 1c), and such wavenumbers are not well represented by the coarse-grained average (Figs. 1a,b).

The values of l and κ_0 determined here, as well as other parameter values used in this paper, are tabulated in Table 1.

4. Geographic distribution of $\mathcal{F}_{4\times}$ with CO_2 only

Now we apply Eq. (7) along with (5) to more realistic atmospheric columns to obtain a geographical distribution of CO_2 forcing. We continue to consider the CO_2-only case, postponing an analysis of the effects of H_2O overlap to sections 5 and 6. We also only consider forcings relative to a uniform, preindustrial values of $q_i = 280$ ppmv.

TABLE 1. Parameters for the simple model of CO_2 forcing. See referenced sections for details.

Description	Symbol, value	Section where described
Wavenumber at band maximum	$\nu_0 = 667.5\,\mathrm{cm}^{-1}$	Section 2
Reference T and p for CO_2 absorption coefficients	$(T_{ref}, p_{ref}) = (250\,\mathrm{K}, 100\,\mathrm{hPa})$	Section 2
Band-maximum reference CO_2 absorption coefficient	$\kappa_0 = 50\,\mathrm{m}^2\,\mathrm{kg}^{-1}$	Section 3b
Spectroscopic decay parameter	$l = 10.2\,\mathrm{cm}^{-1}$	Section 3b
Emission levels	$\tau_{em}^{CO_2} = 0.5$, $\tau_{em}^{H_2O} = 0.6$	Appendix B
Reference T and p for H_2O absorption coefficients	$(T_{ref}^-, p_{ref}^-) = (245\ \mathrm{K},\ 370\ \mathrm{hPa})$	Appendix A
(different for "+" and "−" wavenumber regions)	$(T_{ref}^+, p_{ref}^+) = (275\ \mathrm{K},\ 650\ \mathrm{hPa})$	
Reference RH for continuum absorption in the "+" region	$\mathrm{RH}_{ref} = 0.75$	Appendix A
Reference H_2O absorption coefficients	$\kappa_{ref}^- = 0.1\,\mathrm{m}^2\,\mathrm{kg}^{-1}$ $\kappa_{ref}^+ = 0.025\,\mathrm{m}^2\,\mathrm{kg}^{-1}$	Appendix A
Clausius-Clapeyron scaling coefficient in the "+" region	$\alpha_0 = \dfrac{L}{R_v T_{ref}^{+2}}$	Appendix A
Continuum T scaling for κ^+	$\sigma = 0.021\,\mathrm{K}^{-1}$	Appendix A
T scaling for τ^+	$\alpha = 2\alpha_0 - \sigma$	Appendix A

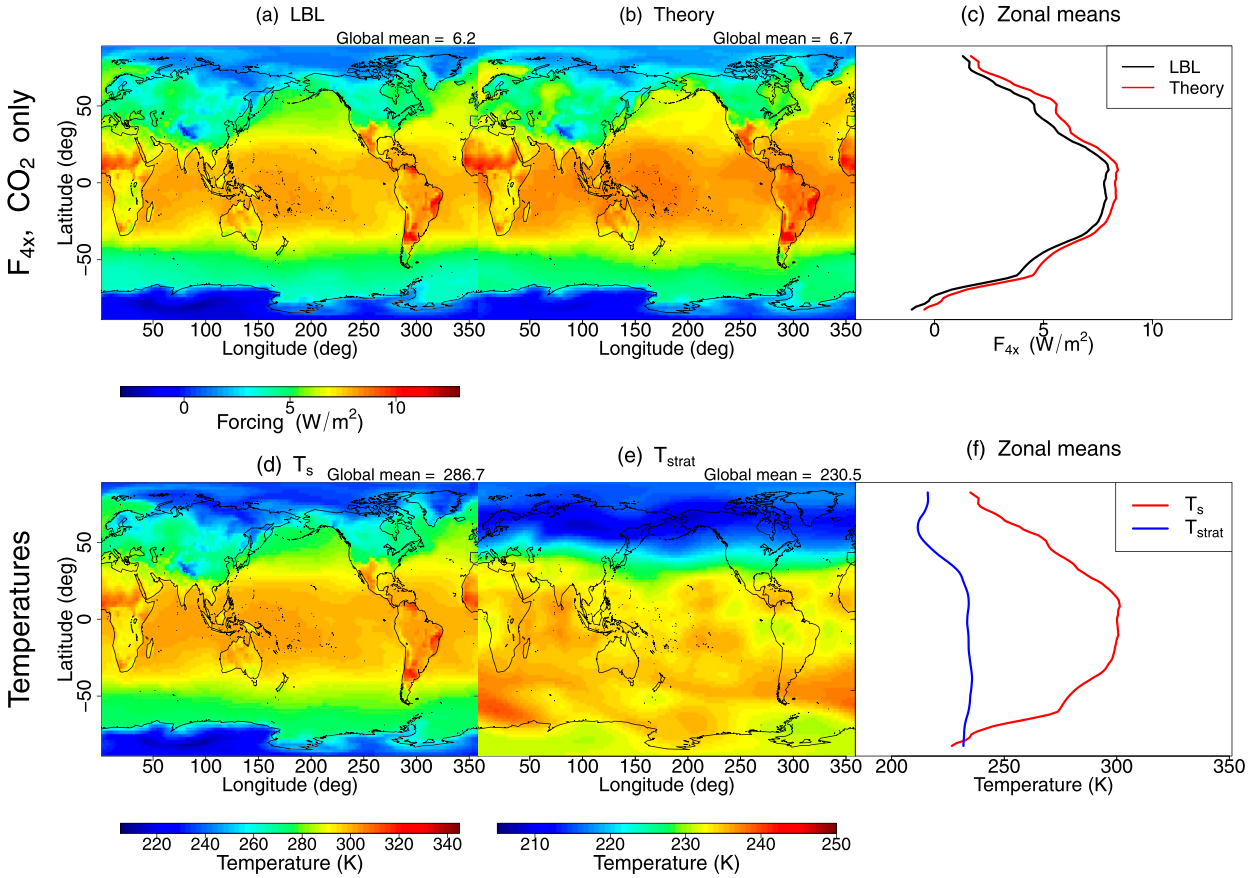

FIG. 3. Maps of (a) CO_2 forcing $\mathcal{F}_{4\times}$ with CO_2 only from a LBL calculation; (b) as in (a), but using Eq. (7); (d) surface temperature T_s; and (e) stratospheric emission temperature T_{strat}, as diagnosed by Eq. (5). (c) Zonal means of (a) and (b); (f) zonal means of (d) and (e). The spatial variations in CO_2 forcing, and in particular the meridional gradient, are captured by the analytical model. Furthermore, the T_s map in (d) is almost identical to the $\mathcal{F}_{4\times}$ maps in (a) and (b), showing that the spatial variations in $\mathcal{F}_{4\times}$ in the CO_2-only case stem almost entirely from T_s, with T_{strat} variations playing a much smaller role. Accordingly, the strong meridional gradient in zonal-mean T_s matches that of $\mathcal{F}_{4\times}$ [(c) and (f)], while the meridional gradient in T_{strat} is weak.

We take as atmospheric data a 22 March 1981 snapshot from a historical run of GFDL's AM3 (Donner et al. 2011). This equinoctial snapshot has meridional temperature gradients typical of the annual mean, but also exhibits zonal variations due to synoptic-scale weather, which provides a more stringent test of our simple model than annual mean fields. We calculate the forcing $\mathcal{F}_{4\times}$ from a quadrupling of CO_2 for each column using our global LBL code as well as Eq. (7), with the results in Figs. 3a–c. Despite its simplicity, Eq. (7) captures the spatial pattern and overall magnitude of CO_2 forcing as calculated by the global LBL, in both the zonal mean and fully spatially resolved ($R^2 = 0.994$ for the latter). The most conspicuous errors are a small overall positive bias, as well as a larger overestimate of the zonal mean forcing near 50°N. Both of these errors appear to be due to the idealization of a single emission pressure p_0 at the center of the CO_2 band; in section 7 we evaluate the tropopause forcing that does not depend on p_0, and these errors disappear (Fig. 10). The larger error near 50°N seems related to a vertical minimum in stratospheric temperatures near p_0 at those latitudes, which biases our estimate of stratospheric emission.

Several other features of Figs. 3a–c deserve mention. As pointed out in the introduction and also found in previous studies (which typically include H_2O and clouds; e.g., H16; Byrne and Goldblatt 2014; Myhre and Stordal 1997), there is a strong meridional gradient in CO_2 forcing, with large values in the tropics and values close to zero or even negative near the poles. [The potentially surprising negative values[6] over Antarctica were emphasized by Schmithüsen et al. (2015), but subsequently put into context by Smith et al. (2018), Flanner et al. (2018), and Freese and Cronin (2021).[7]] There are also several small-scale regions of enhanced forcing throughout the tropics, as well as a diminished forcing over the Tibetan Plateau.

[6] Note that this negative CO_2 forcing is related to, but distinct from, the negative *climatological* greenhouse effect discussed in, e.g., Sejas et al. (2018).

[7] In particular, a negative instantaneous forcing can still lead to a positive surface temperature perturbation, because of stratospheric adjustment as well as surface-troposphere decoupling.

The simplicity of (7) allows us to identify the origin of these and other spatial variations in $\mathcal{F}_{4\times}$. The only spatially varying quantities in (7) are T_s and T_{strat}, which are plotted in Figs. 3d–f. The T_s map is almost identical to the $\mathcal{F}_{4\times}$ maps, showing that the spatial variations in $\mathcal{F}_{4\text{x}}$ in the CO_2-only case stem almost entirely from T_s, with T_{strat} variations playing a much smaller role ($R^2 = 0.961$ between the maps of T_s and LBL $\mathcal{F}_{4\times}$). Accordingly, the strong meridional gradient in zonal mean T_s matches that of $\mathcal{F}_{4\times}$, while the meridional gradient in T_{strat} is weak (Figs. 3c,f) With such weak T_{strat} gradients, both the large-scale meridional gradient in $\mathcal{F}_{4\times}$ as well as the regional features mentioned above can then be understood simply as consequences of variations in surface temperature. (In particular, the negative $\mathcal{F}_{4\times}$ values over Antarctica occur because there we find $T_s < T_{\text{strat}}$.) Physically, surface temperatures are critical because they dictate the strength of the emission blocked by the widened CO_2 band (red lines in Fig. 1a).

5. Theory for $\mathcal{F}_{4\times}$ including H_2O overlap

a. Heuristics

We now consider overlap[8] between the 667 cm^{-1} CO_2 band and the H_2O rotational band and continuum. To get a feel for the impact of H_2O overlap, Fig. 4 shows the zonal mean forcing for our GCM snapshot for both the CO_2-only and H_2O overlap cases, as computed with our global LBL code. It is immediately apparent that H_2O overlap significantly modulates the meridional gradient in CO_2 forcing from the CO_2-only case, by significantly reducing $\mathcal{F}_{4\times}$ in the tropics (H_2O overlap makes little difference in the very dry regions poleward of roughly ±65°). A map of this forcing (Fig. 7a, presented in the next section) also shows zonal asymmetries in tropical $\mathcal{F}_{4\times}$, which appear related to synoptic-scale weather.

To understand these features, we must understand how H_2O changes the heuristic picture of CO_2 forcing in Fig. 1. Returning to our idealized single-column calculations, Fig. 5b shows $p_{\text{em}}(\nu)$ as calculated by RFM for $q = 0$, 280, and 1120 ppmv in our BASE atmospheric column but now in the presence of H_2O. We see that the surface emission from Fig. 1 is replaced by tropospheric emission from H_2O. This should indeed reduce the forcing relative to the CO_2-only case, as increasing CO_2 will now displace H_2O emission from the *atmosphere* rather than warmer surface emission. Furthermore, this displaced H_2O emission will itself depend on relative humidity RH, as drier areas will emit from closer to the surface and hence at warmer temperatures, yielding a stronger forcing; this potentially explains the meridional gradient and zonal asymmetries in tropical $\mathcal{F}_{4\times}$ seen in Figs. 4 and 7a.

[8] Strictly speaking, "overlap" refers to absorption and emission by multiple gases at a given wavenumber, and this is indeed what is modeled in our LBL calculations. The simple model developed below, however, treats wavenumbers as either entirely H_2O or CO_2-dominated, so the simple model idealizes overlap as the presence of wavenumbers that transition from H_2O to CO_2-dominated as CO_2 concentrations are increased.

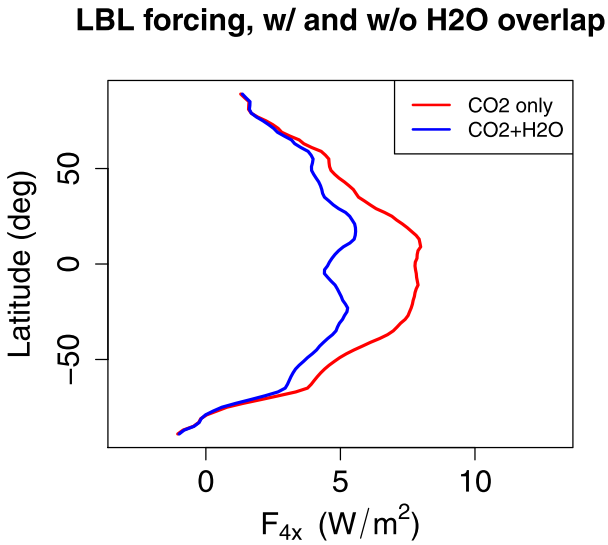

FIG. 4. Zonal mean forcing for our GCM snapshot for both the CO_2-only and H_2O overlap cases, as computed with our global LBL code. H_2O strongly modulates the CO_2 forcing outside the dry polar regions, thus also modulating the meridional gradient in CO_2 forcing.

To construct an analog to Fig. 1a, we first assume that the H_2O emission on each side of the CO_2 band has an (RH-dependent) emission temperature (continuing to make the emission level approximation), and that under an increase in CO_2 it is this emission that will be replaced by stratospheric emission. This idealization is depicted in Fig. 5a. We take the 550–600 cm^{-1} spectral interval to be the low wavenumber side of the CO_2 band, and quantities averaged over or pertaining to this interval will be signified with a minus sign (−); similarly, we take 750–800 cm^{-1} as the high-wavenumber side, and quantities averaged over or pertaining to this interval will be signified with a plus sign (+).

To turn the heuristic picture of Fig. 5a into a formula that generalizes (7), we will estimate spectrally averaged H_2O optical depths $\tau^{\pm}$, which we can combine with an emission level τ^{H2O} to find $T(\tau^{\pm} = \tau_{\text{em}}^{\text{H}_2\text{O}})$. We then invoke Eq. (B4), which says that the emission temperatures may be approximated as the minima of T_s and $T(\tau^{\pm} = \tau_{\text{em}}^{\text{H}_2\text{O}})$:

$$T_{\text{em}}^{\pm} \equiv \min\left[T_s, T\left(\tau^{\pm} = \tau_{\text{em}}^{\text{H}_2\text{O}}\right)\right]. \tag{8}$$

Appendix B derives and validates this emission level approximation, and also derives a value of $\tau_{\text{em}}^{\text{H}_2\text{O}} = 0.6$. This derivation holds only for a single wavenumber, however, and there is an implicit but strong assumption in Eq. (8) that in spectrally averaging Eq. (B4), we may commute the "min" function with the spectral averaging. The limitations of this assumption will become evident below. Regardless, with (8) in hand we may then construct a mean H_2O emission temperature

$$\overline{T}_{\text{em}} \equiv \frac{T_{\text{em}}^{+} + T_{\text{em}}^{-}}{2}, \tag{9}$$

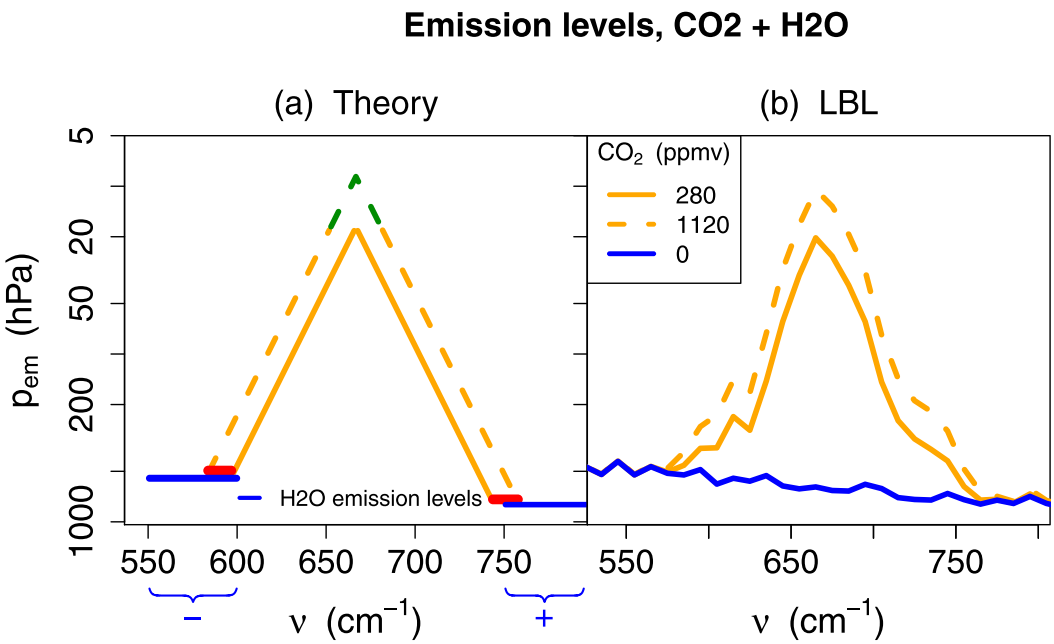

FIG. 5. (a),(b) As in Figs. 1a and 1b but with H_2O overlap, again for the BASE atmosphere. H_2O emission levels are shown in blue; in (a) they are given by Eqs. (12) while in (b) they are diagnosed directly from RFM by $\tau_\nu = 0.5$ and geometrically averaged over 10-cm^{-1} bins, just as for CO_2. Note that (b) shows that the presence of H_2O implies that increasing CO_2 blocks tropospheric H_2O emission rather than surface emission. This is idealized in (a), which assumes a single emission level in each of two spectral regions, denoted "−" and "+" and spanning the wavenumber ranges 550–600 and 750–800 cm^{-1}, respectively.

which can be substituted into (7) for T_s, in line with the heuristic picture in Fig. 5a.

b. Theory

Now we proceed with the quantitative details. The reader uninterested in the following details of H_2O radiative transfer may skip to Eq. (12), which give the desired expressions for $T(\tau^\pm = \tau_{em}^{H_2O})$, and proceed from there.

Since optical depth is a vertical integral of absorber density times absorption coefficient, a prerequisite for calculating $\tau^\pm$ is to obtain estimated, spectrally averaged H_2O absorption coefficients $\kappa^\pm$. A complication, however, is that κ^- is dominated by line absorption, whereas κ^+ is dominated by continuum absorption (Shine et al. 2012; see also appendix A). Accordingly, we approximate κ^- as scaling with foreign pressure broadening only (Pierrehumbert 2010), while κ^+ scales with self-broadening[9] only:

$$\kappa^- = \kappa_{ref}^- \frac{p}{p_{ref}^-}, \tag{10a}$$

$$\kappa^+ = \kappa_{ref}^+ \frac{RH}{RH_{ref}} e^{(\alpha_0 - \sigma)(T - T_{ref}^+)}. \tag{10b}$$

[9] We neglect here the foreign-broadened component of the continuum, which is weaker in the moister, tropical columns where continuum absorption is significant (Shine et al. 2012).

The reference absorption coefficients $\kappa_{ref}^\pm$ are evaluated at distinct reference pressures and temperatures ($p_{ref}^\pm$, $T_{ref}^\pm$), and κ^+ also requires a reference relative humidity RH_{ref}. The constant $\alpha_0 \equiv L/(R_v T_{ref}^{+2})$ results from linearization of the exponent in Clausius–Clapeyron, and $e^{\alpha_0(T - T_{ref}^+)}$ combines with the RH/RH_{ref} factor to give the required vapor pressure scaling [see also Eq. (A1)]. The constant $\sigma = 0.02\,K^{-1}$ is an explicit temperature scaling coefficient. Equation (10b) and the parameter values therein are derived in detail and evaluated in appendix A. Parameter values are recorded in Table 1.

The approximations (10) then allow for an analytical evaluation of $\tau^\pm$, as follows. We integrate using temperature as our dummy integration variable, and set the lower bound of the integral to the cold-point tropopause temperature T_{tp} whose H_2O concentrations are assumed negligible (here and below we take the cold point as the tropopause). For τ^-, which we model as being due to line absorption, such a calculation was already performed in Jeevanjee and Fueglistaler (2020b), so we simply quote their Eq. (12):

$$\tau^- = D\kappa_{ref}^- \frac{p}{p_{ref}^-} WVP_0 \exp\left(-\frac{L}{R_v T}\right), \tag{11a}$$

where $WVP_0 = (T_s + T_{tp})RH p_v^\infty/(2\Gamma L)$ depends on RH and has units of water vapor path, $p_v^\infty = 2.5 \times 10^{11}$ Pa, the saturation vapor pressure $p_v^*(T) = p_v^\infty \exp(-L/R_v T)$, and all other symbols have their usual meaning.

For τ^+, the self-broadening scaling, (10b), makes for a different calculation. Denoting vapor density by ρ_v [kg m^{-3};

saturation value is denoted with an asterisk (*)] and noting that $\rho_v(T) \approx \rho_v(T^+_{\rm ref}) \exp[\alpha_0(T - T^+_{\rm ref})]$, we have

$$\tau^+ = D\int_{T_{\rm tp}}^{T} \kappa^+ \rho_v \frac{dT'}{\Gamma}$$
$$\approx D\frac{\mathrm{RH}^2}{\mathrm{RH}_{\rm ref}}\rho_v^*(T^+_{\rm ref})\int_{T_{\rm tp}}^{T}\kappa^+_{\rm ref}e^{\alpha(T'-T^+_{\rm ref})}\frac{dT'}{\Gamma},$$
$$= D\frac{\mathrm{RH}^2\rho_v^*(T^+_{\rm ref})\kappa^+_{\rm ref}}{\mathrm{RH}_{\rm ref}\Gamma\alpha}e^{\alpha(T-T^+_{\rm ref})}, \tag{11b}$$

where $\alpha \equiv 2\alpha_0 - \sigma$.

Inverting Eqs. (11) at $\tau^\pm = \tau^{\rm H_2O}_{\rm em}$ then yields [employing the Lambert W function that satisfies $W(xe^x) = x$]

$$T(\tau^- = \tau^{\rm H_2O}_{\rm em}) = \frac{T^*}{W\left[\frac{T^*}{T^-_{\rm ref}}(D\,\mathrm{WVP}_0\kappa^-_{\rm ref}/\tau_{\rm em})^{R_d\Gamma/g}\right]},$$
$$\text{where}\quad T^* \equiv \frac{LR_d\Gamma}{gR_v} \tag{12a}$$

$$T(\tau^+ = \tau^{\rm H_2O}_{\rm em}) = T^+_{\rm ref} + \frac{1}{\alpha}\ln\left[\frac{\tau_{\rm em}\Gamma\alpha\mathrm{RH}_{\rm ref}}{D\mathrm{RH}^2\rho_v^*(T^+_{\rm ref})\kappa^+_{\rm ref}}\right]. \tag{12b}$$

Note the dependence of $T(\tau^+ = \tau^{\rm H_2O}_{\rm em})$ on RH^2 in (12b), characteristic of the continuum. Equation (12) provides the expressions we seek, and will be combined below with Eqs. (8) and (9) to yield a generalization of (7) valid in the presence of H_2O.

Before validating these expressions for $T(\tau^\pm = \tau^{\rm H_2O}_{\rm em})$ and hence $T^\pm_{\rm em}$, we return to the topic of Simpson's law. As first noted by Simpson (1928), H_2O optical depth at a given wavenumber and at fixed RH is to a first approximation a function of temperature only, due to the dominant influence of Clausius-Clapeyron scaling. This means that $T(\tau_{\rm em})$ for that wavenumber is fixed, and hence *does not depend on* T_s; it is this T_s invariance of H_2O emission temperatures that we refer to as Simpson's law (Jeevanjee et al. 2021). Indeed, Simpson's law can be seen in Eqs. (11) and (12), which do not exhibit any explicit T_s dependence. While Simpson's law is known to have various implications for other aspects of climate,[10] we will see that for CO_2 forcing it leads to an *upper limit* on CO_2 forcing with respect to T_s variations, which appears to be reached in the present-day tropics.

c. Validation

We validate the expressions (8) and (12) for $T^\pm_{\rm em}$ by comparing them to the spectral average of

$$T_{\rm em}(\nu) \equiv \min[T_s, T(\tau_\nu = \tau_{\rm em})] \tag{13}$$

as calculated from RFM output for our single columns with $T_s = 300$ K, no CO_2, and with varying RH. The ground truth $\int T_{\rm em}(\nu)\,d\nu$ for $T^\pm_{\rm em}$ is compared to our estimates from (8) and (12) in Figs. 6a and 6b, which show that Eqs. (8) and (12) do an excellent job of capturing the variation of $T^-_{\rm em}$ with RH, and do a good job with $T^+_{\rm em}$ down to RH values near 0.25, around which a significant fraction of wavenumbers in the "+" spectral region become optically thin and thus have $T_{\rm em}(\nu) = T_s$. In this case the "min" function in (13) does not commute with the spectral averaging, violating the assumption behind (8).

With some confidence in our estimate of $T^\pm_{\rm em}$, we now substitute $\overline{T}_{\rm em}$ from Eq. (9) into Eq. (7) to obtain an expression for CO_2 forcing in the presence of H_2O overlap:

$$\mathcal{F} = 2l\ln\left(\frac{q_f}{q_i}\right)[\pi B(\nu_0, \overline{T}_{\rm em}) - \pi B(\nu_0, T_{\rm strat})] \quad (\mathrm{w/\,H_2O\ overlap}). \tag{14}$$

Note that as RH $\to$ 0, $\overline{T}_{\rm em} \to T_s$ so this equation indeed generalizes (7).

As a preliminary test of (14) we take our single-column, $T_s = 300$ K, variable RH calculations (with $q_i = 280$ ppmv) and compare $\mathcal{F}_{4\times}$ as calculated from RFM with $\mathcal{F}_{4\times}$ calculated from (14) and (12). The result is shown in Fig. 6c and shows quite good agreement between the two, although the errors in $T^+_{\rm em}$ at low RH discussed above do lead to small ($\sim$0.5 W m^{-2}) errors in $\mathcal{F}_{4\times}$.

6. Geographic distribution of $\mathcal{F}_{4\times}$ with H_2O overlap

We now estimate $\mathcal{F}_{4\times}$ with H_2O overlap for our GCM snapshot using Eqs. (8), (9), (12), and (14), where Γ in Eq. (12) is diagnosed for each column as a mass-weighted tropospheric average,[11] and column RH is diagnosed for each GCM column as the precipitable water in the troposphere divided by its saturation value. The results of this computation are shown in Figs. 7b and 7c, and show that Eqs. (7) and (12) indeed capture the spatial distribution and overall magnitude of $\mathcal{F}_{4\times}$ with H_2O overlap, with similar agreement to the CO_2-only case. This supports the heuristic picture of Fig. 5a, namely that the effect of H_2O on CO_2 forcing can be thought of as simply a change in the intensity of the emission (i.e., the $T_{\rm em}$) blocked by CO_2.

We now return to the T_s invariance of $T(\tau^\pm = \tau_{\rm em})$ in Eq. (12). One consequence of this T_s invariance, in combination with Eq. (14), is that while CO_2-only forcing (at fixed q_i) grows with increasing T_s (Fig. 2a), forcing with H_2O overlap should asymptote to a constant value of (14) evaluated on the average of the temperatures in Eq. (12) (assuming fixed RH and $T_{\rm strat}$). We confirm this in Fig. 8, which shows $\mathcal{F}_{4\times}$

[10] For example, there are far-reaching implications for the runaway greenhouse (Nakajima et al. 1992), outgoing longwave radiation (Koll and Cronin 2018), radiative cooling and precipitation (Jeevanjee and Romps 2018), and the water vapor feedback (Ingram 2010; Jeevanjee 2018; Jeevanjee et al. 2021).

[11] More precisely, Γ is obtained as a mass-weighted average between the cold-point tropopause and either 1) the surface or 2) the highest temperature inversion below the cold point (e.g. a trade inversion). The sensitivity to Γ is minor and almost identical results can be obtained with a uniform $\Gamma = 6.5$ K km^{-1}.

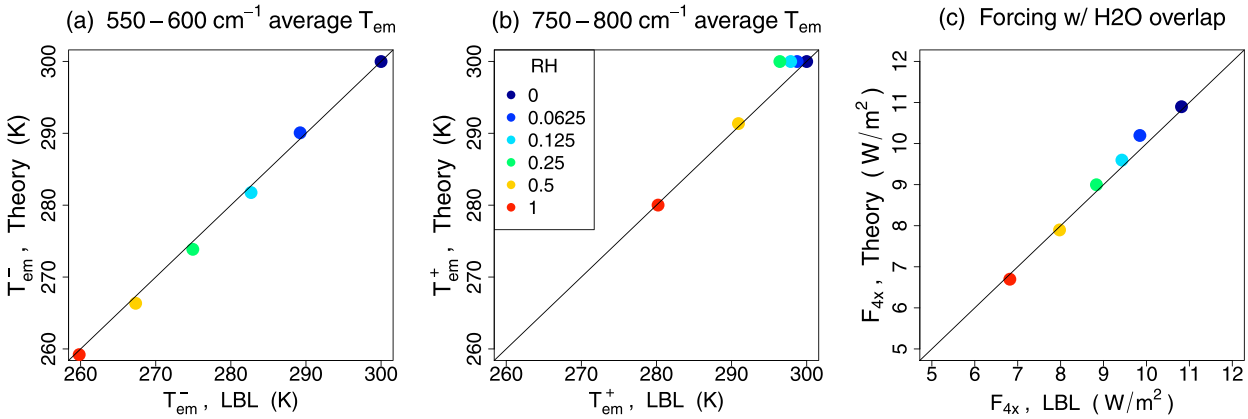

FIG. 6. (a),(b) Validation of our simple expressions (8) and (12) for band-averaged H_2O emission temperatures, as compared to the band average of (13) from RFM. This comparison is made for idealized atmospheric columns with $T_s = 300$, no CO_2, and varying RH. (c) Validation of the simple model (14) for $\mathcal{F}_{4\times}$ in the presence of H_2O, as compared to $\mathcal{F}_{4\times}$ calculated by RFM. This comparison is made for idealized atmospheric columns with $T_s = 300$, $q_i = 280$ ppmv, and varying RH. The simple expressions (8) and (12) predict $T^{\pm}_{em}$ very well except at low RH in the "+" region, leading to small (~0.5 W/m^2) errors in $\mathcal{F}_{4\times}$ at these RH values.

calculated from both RFM as well as Eqs. (7) and (12), for a series of our idealized atmospheric columns with variable T_s and fixed $q_i = 280$ ppmv and RH = 0, 0.75. These plots confirm that the presence of H_2O sets an upper limit on $\mathcal{F}_{4\times}$ with respect to T_s which is well captured by our analytical model. Physically, as T_s increases so does the water vapor path and hence the H_2O optical thickness at all wavenumbers. There is thus a transition in the origin of the emission blocked by increasing CO_2, from surface emission to emission from H_2O, the latter of which is T_s invariant. In reality this occurs at different water vapor paths for different wavenumbers, and thus in the spectral integral this transition is smooth and begins even at

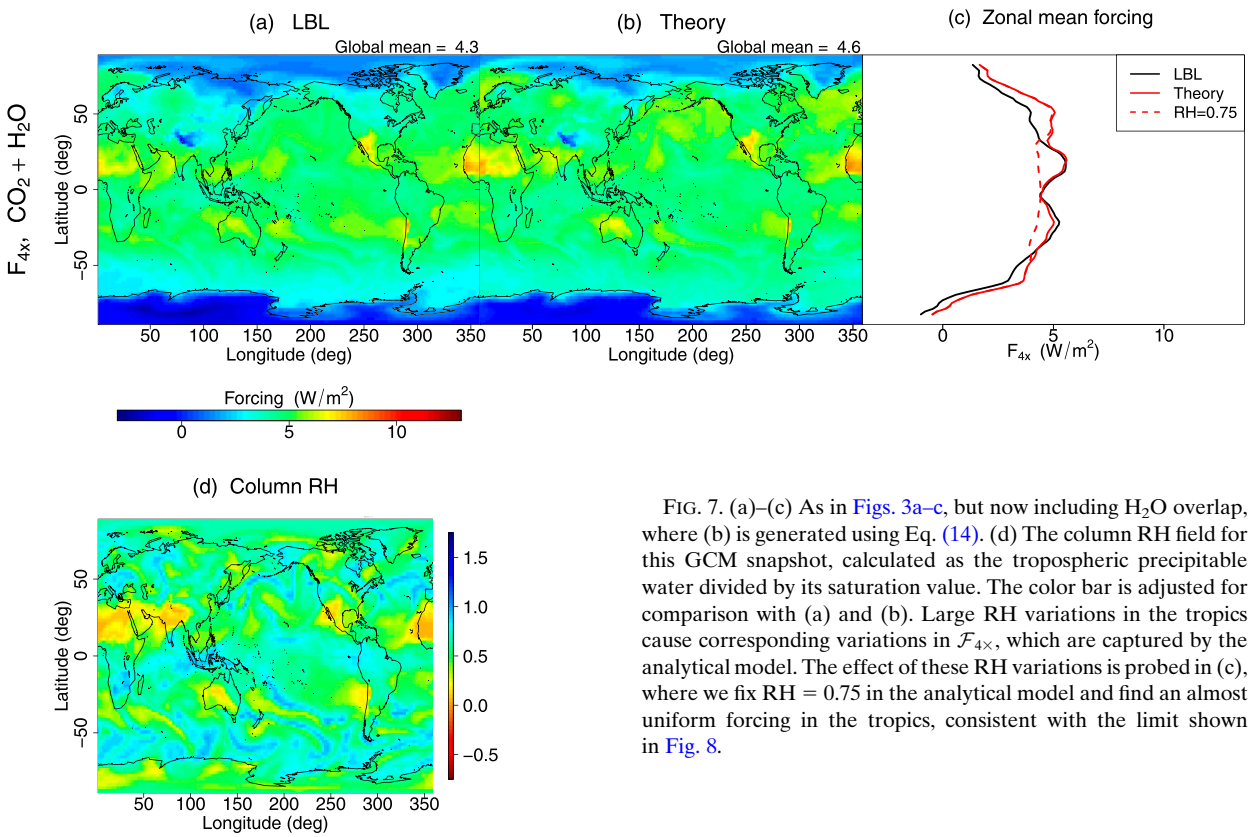

FIG. 7. (a)–(c) As in Figs. 3a–c, but now including H_2O overlap, where (b) is generated using Eq. (14). (d) The column RH field for this GCM snapshot, calculated as the tropospheric precipitable water divided by its saturation value. The color bar is adjusted for comparison with (a) and (b). Large RH variations in the tropics cause corresponding variations in $\mathcal{F}_{4\times}$, which are captured by the analytical model. The effect of these RH variations is probed in (c), where we fix RH = 0.75 in the analytical model and find an almost uniform forcing in the tropics, consistent with the limit shown in Fig. 8.

T_s = 250 K (blue dots in Fig. 8). In our analytical model, however, this transition can only occur separately for the "−" and "+" regions [Eq. (12)] so this transition is more abrupt (blue curve in Fig. 8). Indeed, the kinks in the blue curve in Fig. 8 arise precisely from the kink in the emission level approximation shown in the right panel of Fig. B1.

The limit seen in Fig. 8 is reached beginning at roughly $T_s \approx$ 300 K, a typical T_s of the present-day tropics. This suggests that the forcing curves in the tropics in Fig. 7c may be thought of as having attained a global maximum (for RH ≈ 0.75), with further local maxima in the subtropics arising only from the low RH values there. Indeed, recalculating $\mathcal{F}_{4\times}$ for our GCM snapshot using (14) and (12) but fixing RH = 0.75 yields the dashed red curve, which varies very little across the tropics. Comparison of the $\mathcal{F}_{4\times}$ and RH maps in Fig. 7 shows that the zonal asymmetries in tropical $\mathcal{F}_{4\times}$ are also due to zonal asymmetries in RH, due to the intrusion of deep tropical moisture filaments into the subtropics (e.g., Pierrehumbert and Roca 1998; Pierrehumbert 1998).

It is important to note that this upper limit on CO_2 forcing is with respect to T_s variations only, and assumes a fixed preindustrial baseline concentration q_i as well as a fixed T_{strat}. Increasing q_i much beyond preindustrial values brings secondary CO_2 bands with much weaker H_2O overlap into play (Zhong and Haigh 2013), and this limit then no longer applies.

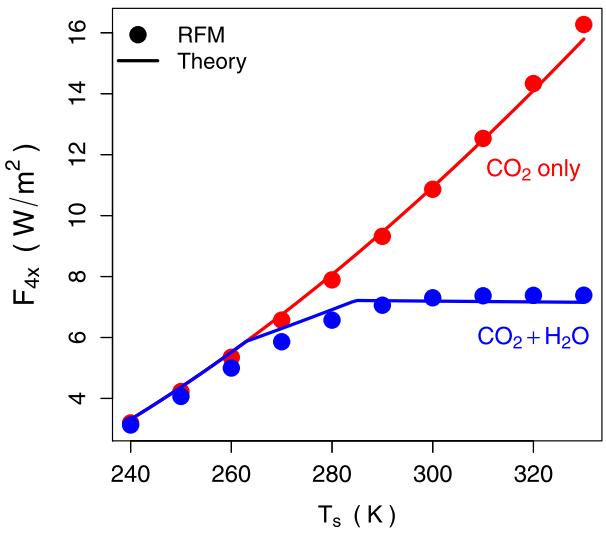

FIG. 8. CO_2 forcing $\mathcal{F}_{4\times}$ for our idealized atmospheric columns with varying T_s and all other parameters fixed at the BASE values. The presence of H_2O (blue) sets a limit on $\mathcal{F}_{4\times}(T_s)$ which does not exist in the CO_2-only case (red). These behaviors are well captured by the analytical model [lines, given by Eqs. (14) and (7)]. The kinks in the blue lines are consequences of employing the emission level approximation [cf. Fig. B1].

7. Tropopause forcing

So far we have focused solely on instantaneous TOA forcing, as it is the simplest version of CO_2 forcing to compute numerically. But as discussed in the introduction, the stratosphere-adjusted forcing has long been recognized to be more directly related to surface warming (e.g., Hansen et al. 1997; IPCC 1994; Rind and Lacis 1993). While calculating stratospheric adjustments is outside the scope of this paper, we can improve upon the instantaneous TOA forcing by considering the instantaneous *tropopause* forcing $\mathcal{F}^{\text{tp}}$, which is well known to be a better approximation to the stratosphere-adjusted forcing. In this section we develop an analytical model for $\mathcal{F}^{\text{tp}}$ analogous to Eq. (7), and ask whether our conclusions from previous sections hold for $\mathcal{F}^{\text{tp}}$ as well.

To describe $\mathcal{F}^{\text{tp}}$ we must estimate both upwelling and downwelling fluxes at the tropopause. For this we need the corresponding emission pressures $p_{\text{em}}^{\uparrow}$ and $p_{\text{em}}^{\downarrow}$, which lie at an optical distance of τ_{em} below and above the tropopause, respectively (in height). These are determined by the equations

$$\tau(p_{\text{em}}^{\uparrow}) = \tau(p_{\text{tp}}) + \tau_{\text{em}}, \tag{15a}$$

$$\tau(p_{\text{em}}^{\downarrow}) = \tau(p_{\text{tp}}) - \tau_{\text{em}}, \tag{15b}$$

where p_{tp} is the tropopause pressure. These equations can be solved numerically from RFM output at each wavenumber, or evaluated analytically using (2), the latter of which yields

$$p_{\text{em}}^{\uparrow} = \sqrt{p_{\text{tp}}^2 + \frac{2gp_{\text{ref}}\tau_{\text{em}}}{D\kappa(\nu)q}}, \tag{16a}$$

$$p_{\text{em}}^{\downarrow} = \sqrt{p_{\text{tp}}^2 - \frac{2gp_{\text{ref}}\tau_{\text{em}}}{D\kappa(\nu)q}}. \tag{16b}$$

These numerical and analytical emission pressures are plotted in Figs. 9a and 9b for the tropopause pressure p_{tp} = 130 hPa from our BASE profile and for CO_2 only, continuing to use $\tau_{\text{em}}^{CO_2} = 0.5$. The corresponding fluxes at the tropopause are shown in Figs. 9c and 9d, where the analytical fluxes are computed as $\pi B[\nu_0, T(p_{\text{em}}^{\uparrow\downarrow})]$, from both RFM output and the analytical expressions (16).

Figure 9 serves two purposes. First, it shows that our analytical formalism captures the first order behavior of the tropopause emission pressures and hence fluxes, just as it does at the TOA. Second, it allows us to heuristically derive an expression for $\mathcal{F}^{\text{tp}}$, as follows. From Fig. 9c, the forcing from the upwelling (red lines) is given by Eq. (7); indeed, this figure gives another heuristic derivation of (7). But, the downwelling contribution to the forcing in Fig. 9c cancels the stratospheric term in (7), leaving only the surface term. This argument extends straightforwardly to the case with H_2O overlap, where T_s must be replaced by $\overline{T}_{\text{em}}$ but the cancellation of the stratospheric term still holds. The tropopause forcing is thus

$$\mathcal{F}^{\text{tp}} = 2l\ln(q_f/q_i)\pi B(\nu_0, \overline{T}_{\text{em}}). \tag{17}$$

Equation (17) is quite striking, in that it says that *the instantaneous tropopause forcing is independent of stratospheric temperatures*. Physically, this arises because the additional (in the same sense as Fig. 1) upwelling and downwelling shown in Fig. 9 both originate from very near the tropopause, and thus have emission temperatures nearly equal to the tropopause temperature and thus cancel.

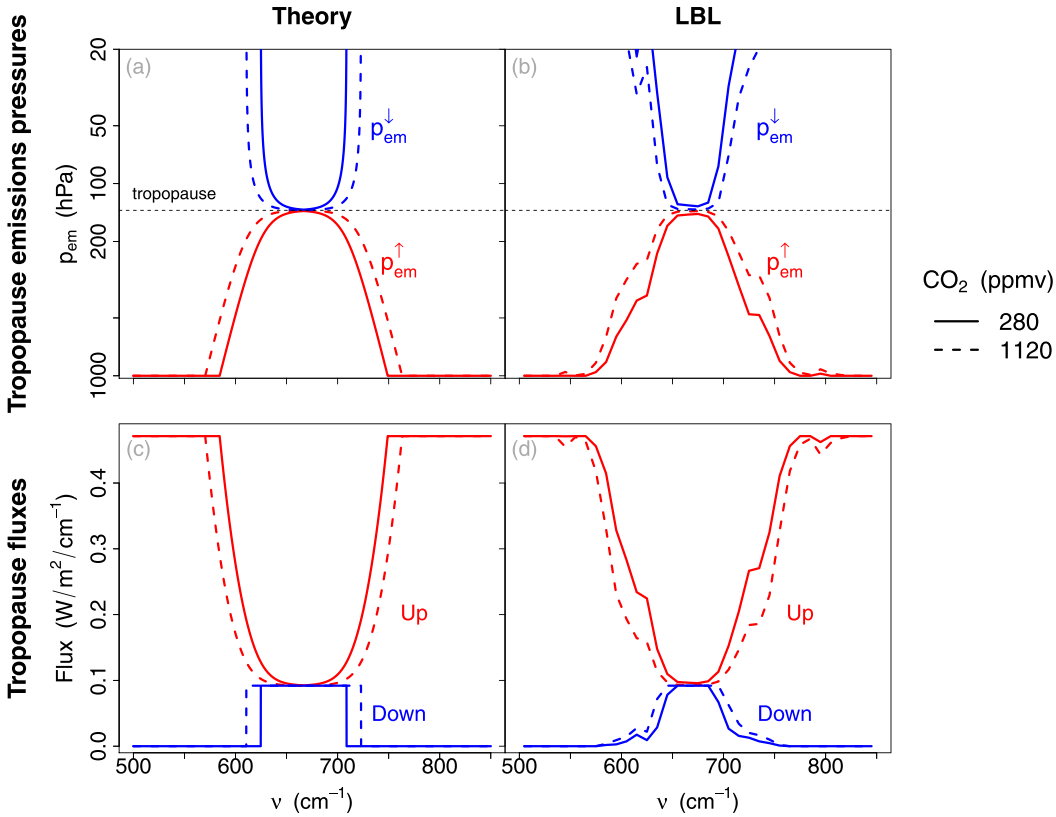

FIG. 9. (a),(b) Emission levels $p_{em}^{\uparrow\downarrow}$ as seen from the tropopause as defined by Eq. (15), evaluated (a) analytically using Eq. (16) and (b) numerically from RFM output, for $q = 280$ (dashed) and 1120 ppmv (dashed) and the BASE atmosphere. Levels $p_{em}^{\downarrow}$ emitting downward toward the tropopause are shown in blue, and levels $p_{em}^{\uparrow}$ emitting upward toward the tropopause in red. (c),(d) As in (a) and (b), but for the corresponding upwelling and downwelling spectral fluxes. The comparison between theory and LBL output validates the theory, to first order. Furthermore, the change in upwelling flux [red lines in (c)] can be estimated as that given by Eq. (7), but there is an additional compensating change in downwelling radiance [blue lines in (c)], yielding the instantaneous tropopause forcing, (17).

To test Eq. (17), we repeat the global calculations of $\mathcal{F}_{4\times}$ shown in Figs. 3 and 7, but now for the tropopause forcing $\mathcal{F}_{4\times}^{tp}$ where we take the tropopause in each column to be the cold point. The result is shown in Fig. 10. The agreement in both the CO_2-only and H_2O overlap cases is excellent. Interestingly, the accuracy of the analytical model is better for $\mathcal{F}_{4\times}^{tp}$ than $\mathcal{F}_{4\times}$ (cf. Fig. 3), because there is no stratospheric term in (17) and thus no errors arising from the idealization of a single "peak" emission pressure p_0 [cf. Eqs. (3) and (5)].

Although the instantaneous tropopause forcing $\mathcal{F}^{tp}$ is independent of stratospheric temperature, the *adjusted* tropopause forcing will of course depend on the stratospheric temperature adjustment, as this will change the downwelling but not the upwelling at the tropopause. This upsets the cancellation of the added upwelling and downwelling described above. But, it turns out that the adjustment to tropopause forcing from changes in lower stratospheric downwelling is much smaller (10%–15%) than the adjustment to TOA forcing from changes in upper stratospheric upwelling (30%–40%) (e.g., Richardson et al. 2019). This is presumably because the stratospheric temperature adjustment is much more pronounced in the upper rather than lower stratosphere (Wang and Huang 2020). Thus $\mathcal{F}^{tp}$ is a good (i.e., to within 15%) estimate of the adjusted forcing, and the stratospheric adjustment can be considered a relatively minor correction. Furthermore, since $\mathcal{F}^{tp}$ depends solely on T_s and not on T_{strat}, the claim that the meridional gradient in CO_2 forcing is largely governed by the meridional T_s gradient is even more accurate for $\mathcal{F}^{tp}$ than $\mathcal{F}$. All of this suggests that our conclusion that spatial variations in CO_2 forcing are due predominantly to surface temperature variations, with modulation by H_2O, should hold for stratosphere adjusted forcing as well as the instantaneous forcings considered here.

8. Summary and discussion

We summarize our main results as follows:

- Clear-sky TOA CO_2 forcing $\mathcal{F}$ in the absence of H_2O can be viewed as a swap of surface emission for stratospheric emission [Fig. 1a, Eq. (7)]. Thus, $\mathcal{F}$ is governed by surface–stratosphere temperature contrast, and the strong meridional

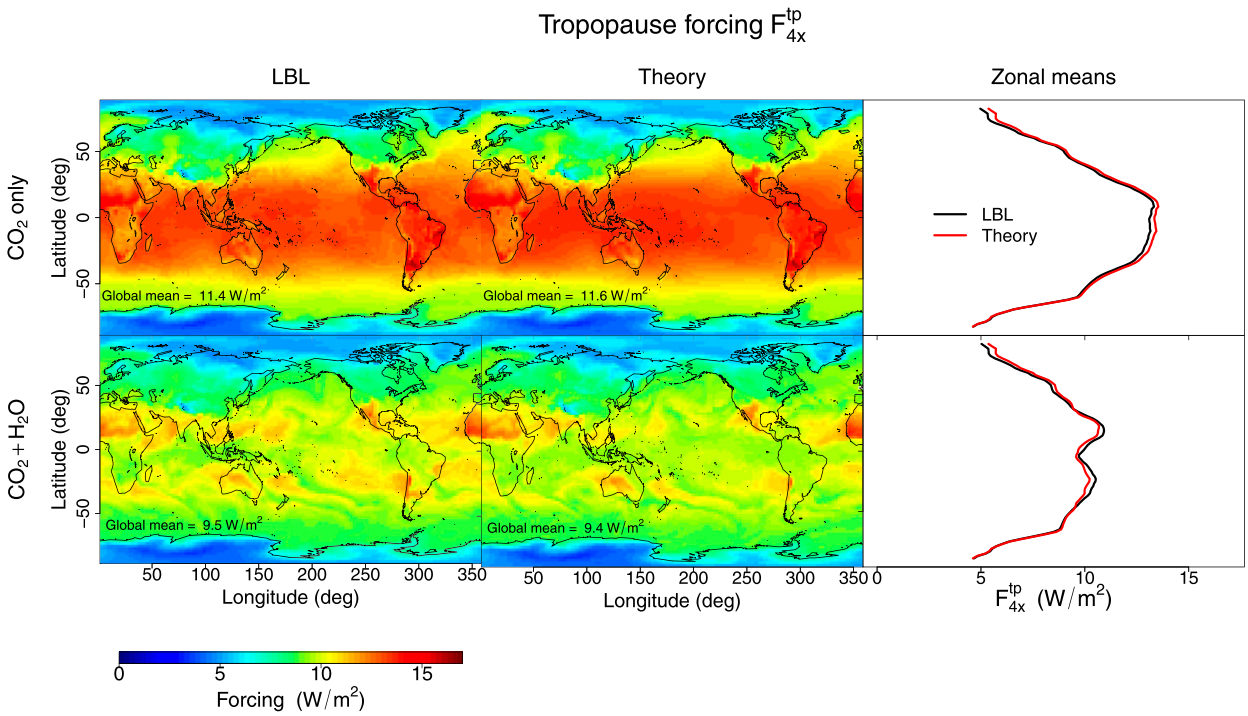

FIG. 10. Spatial distributions of tropopause forcing $\mathcal{F}_{4\times}^{tp}$, (top) with CO_2 only and (bottom) with H_2O overlap, from (left) our global LBL calculation and (center) Eq. (17), along with (right) zonal means. The excellent agreement between the LBL calculation and Eq. (17) validates the claim that instantaneous tropopause forcing is independent of stratospheric temperature. The spatial variations seen here are thus determined entirely by T_s with modulation by H_2O, even more so than for the TOA forcings of Fig. 3 and 7.

gradient in $\mathcal{F}$ can be attributed largely to the meridional gradient in surface temperature (Fig. 3).

- The meridional forcing gradient is significantly modulated by the presence of H_2O (Fig. 4), where H_2O replaces surface emission at the edges of the CO_2 band with colder atmospheric emission (Fig. 5).
- The T_s invariance of H_2O emission temperatures $T_{em}^{\pm}$ implies an upper limit (at fixed RH and with respect to T_s variations) on CO_2 forcing (Fig. 8). This limit is likely reached in the present-day tropics (Fig. 7).

We also considered the instantaneous tropopause forcing $\mathcal{F}^{tp}$ and found that it depends on T_s only, so the above conclusions also hold (perhaps even more so) for $\mathcal{F}^{tp}$. However, it would still be useful in future work to calculate the full stratosphere-adjusted rather than instantaneous forcings, using perhaps a simple method for the stratospheric adjustment such as fixed dynamical heating (Fels et al. 1980).

Another extension of this work would be to generalize Eq. (7) to cloudy columns, and hence to compute all-sky forcing. This might be accomplished by replacing T_s with a diagnosed cloud-top temperature, just as we replaced T_s by T_{em} in the presence of H_2O. Clouds, like H_2O, should simply change the upwelling radiation that is blocked by additional CO_2. This is already well known in the literature as the "cloud masking" of CO_2 forcing (e.g., H16), but might be succinctly and quantitatively described by the substitution of cloud-top temperature for T_s in (7). Such an approach, applied to feedbacks rather than forcing, was recently taken in McKim et al. (2021).

Although this work focuses on the spatial variations of CO_2 forcing, the physics of these variations is simply the atmospheric state dependence of CO_2 forcing, which also has implications for CO_2 forcing as a function of base climate. For instance, a very cold Snowball Earth climate (e.g., Hoffman et al. 2017) will have negligible H_2O and a much smaller surface–stratosphere temperature contrast, which would lead to much reduced CO_2 forcings relative to the present day. This fact and its implications for exiting the Snowball Earth state were noted by Pierrehumbert (2004), but Eq. (7) makes this precise and allows for quantitative estimates of this effect.

The state dependence of CO_2 forcing may also be relevant to the spread in CO_2 forcing among GCMs (e.g., Soden et al. 2018; Chung and Soden 2015a,b; Zhang and Huang 2014). This spread is often attributed to parameterization error in GCM broadband radiation schemes, but may also have a contribution from spread in GCM base states. Equation (14) is computationally inexpensive to evaluate (no spectral or vertical integration required) and thus might be applied to GCM output to estimate this contribution. Indeed, one can simply differentiate (7) with respect to T_s and evaluate at $T_s = 288\,\mathrm{K}$, obtaining $2l(\ln 2)\pi(\partial B/\partial T)(\nu_0, 288\,\mathrm{K}) = 0.070\,\mathrm{W\,m^{-2}\,K^{-1}}$ for CO_2 doubling. Thus, biases of 2 K in T_s (Flato et al. 2013) should bias $\mathcal{F}_{2\times}$ by roughly $0.14\,\mathrm{W\,m^{-2}}$. One can also consider T_{strat} biases, which by a similar differentiation of (7) but with

respect to $T_{\rm strat}$ and evaluated at $T_{\rm strat} = 220\,{\rm K}$ yields a sensitivity of $-0.04\,{\rm W\,m^{-2}\,K^{-1}}$. Biases of 4–5 K in $T_{\rm strat}$ (Butchart et al. 2011) would thus similarly bias $\mathcal{F}_{2\times}$ by 0.1–0.2 $\rm W\,m^{-2}$. Note that these sensitivities to T_s and $T_{\rm strat}$ mean that $\mathcal{F}$ is not entirely independent of the warming it produces, thus measuring the degree to which the usual forcing-feedback framework is only an approximation.

Finally, it is worth noting that our analytical model can explain empirically determined features of the linear regression model of H16. For example, p_0 (280 ppmv) = 16 hPa from (3) is close to the empirically determined 10-hPa value used in H16 to evaluate stratospheric temperatures. As another example, consider H16's T_s regression coefficient of $0.066\,{\rm W\,m^{-2}\,K^{-1}}$ for CO_2 doubling. According to our model, this coefficient should simply be the $0.070\,{\rm W\,m^{-2}\,K^{-1}}$ calculated in the previous paragraph, a close numerical agreement.

Acknowledgments. NJ thanks Yi Huang for discussions, Robert Pincus and V. Ramaswamy for encouragement, and W. Happer for discussion of CO_2 spectroscopy and for pointing out the Wilson and Gea-Banacloche (2012) reference. The authors thank five anonymous reviewers as well as Pu Lin and Mike Winton for detailed feedback on the manuscript at various stages. NJ was supported by a Harry Hess post-doctoral fellowship from Princeton Geosciences, JS is supported by a HUCE fellowship, and SF acknowledges support from NSF Grants 1660538 and 1733818.

APPENDIX A

Estimate for H_2O Self-Broadened Absorption Coefficient

This appendix discusses our determination of the spectrally averaged reference absorption coefficients $\kappa^{\pm}_{\rm ref}$ appearing in (10), and also derives the expression (10b) for the self-broadened absorption coefficient profile κ^+.

Self-broadened continuum H_2O absorption coefficients exhibit both an explicit temperature scaling and pressure broadening, the latter of which scales linearly with *vapor* pressure p_v rather than the dry air pressure p (Pierrehumbert 2010). These scalings are thus relative to a reference temperature and reference vapor pressure, the latter of which can be written in terms of the saturation vapor pressure p_v^* and reference RH as $p_{v,\rm ref} = {\rm RH}_{\rm ref} p_v^*(T_{\rm ref})$. The vapor pressure scaling can then be written as

$$\frac{p_v}{p_{v,\rm ref}} = \frac{{\rm RH} p_v^*(T)}{{\rm RH}_{\rm ref} p_v^*(T_{\rm ref})} \approx \frac{\rm RH}{{\rm RH}_{\rm ref}} e^{\alpha_0 (T - T_{\rm ref})}, \quad \text{where} \quad \alpha_0 \equiv \frac{L}{R_v T_{\rm ref}^2}. \tag{A1}$$

As for the explicit temperature scaling, this takes the form $e^{\sigma(T_{\rm ref} - T)}$ (Mlawer et al. 2012).

Since the "+" wavenumber region is dominated by continuum absorption (as we will see), we will adopt the above vapor pressure scaling for κ^+, as well as the explicit temperature scaling coefficient $\sigma = 0.021\,{\rm K^{-1}}$ relevant for this wavenumber region (Mlawer et al. 2012). We specify reference values ${\rm RH}_{\rm ref} = 0.75$ and $T^+_{\rm ref} = 275\,{\rm K}$ for κ^+, and $(p^-_{\rm ref}, T^-_{\rm ref}) = (370\,{\rm hPa}, 245\,{\rm K})$ for κ^-, which will scale with the dry air pressure [Eq. (10a)]. These reference pressures and temperatures are in principle arbitrary, but values near the emission pressures and temperatures can be expected to minimize errors from our various approximations. We can now write down κ^+ as

$$\kappa^+ = \kappa^+_{\rm ref} \frac{\rm RH}{{\rm RH}_{\rm ref}} e^{(\alpha_0 - \sigma)(T - T^+_{\rm ref})}. \tag{A2}$$

This is Eq. (10b) in the main text. Equation (10a) is standard and can be found in textbooks (e.g., Pierrehumbert 2010), although it neglects temperature scaling of line absorption, an issue to which we return below.

To gauge the accuracy of Eq. (10), Fig. A1 shows profiles of spectrally averaged total absorption coefficient $\kappa_{\rm tot}$, lines-only contribution $\kappa_{\rm lines}$, and the difference $\kappa_{\rm ctm}$, which we can ascribe to the continuum, for both the "+" and "−" wavenumber regions. These profiles are calculated via RFM for our BASE column, where $\kappa_{\rm lines}$ is calculating by running RFM without continuum effects, and all spectral averages are performed geometrically rather than arithmetically. Figure 8 shows that for our BASE column the continuum contribution $\kappa_{\rm ctm}$ dominates in the "+" region but not in the "−" region, justifying our use of continuum scalings for the "+" region only. This figure also shows our estimates (10), with $\kappa^{\pm}_{\rm ref}$ taken to be equal to $\kappa^{\pm}_{\rm tot}(p^{\pm}_{\rm ref}, T^{\pm}_{\rm ref}, {\rm RH}_{\rm ref})$, yielding $\kappa^-_{\rm ref} = 0.1\,{\rm m^2\,kg^{-1}}$ and $\kappa^+_{\rm ref} = 0.025\,{\rm m^2\,kg^{-1}}$. Our estimates (10) thus agree with $\kappa^{\pm}_{\rm tot}$ at $(p^{\pm}_{\rm ref}, T^{\pm}_{\rm ref}, {\rm RH}_{\rm ref})$ by construction, but due to the many approximations we have made do not have the same logarithmic slope (i.e., scaling) as $\kappa_{\rm tot}$. However, because H_2O optical depth is an integral of $\kappa_{\rm tot}$ weighted by p_v, Clausius–Clapeyron scaling means it is only important for κ to have the right order of magnitude in the range of $(T_{\rm em} - 20\,{\rm K}, T_{\rm em})$ or so, within which our estimates are accurate to roughly a factor of 2 (by our choice of $T^{\pm}_{\rm ref}$).

It is interesting to note that the logarithmic slopes of $\kappa_{\rm lines}$ and $\kappa_{\rm etm}$ are comparable for a given wavenumber range, despite the naive expectation that $\kappa_{\rm lines}$ scales with p (which varies by a factor of 5 over the vertical range shown in Fig. A1) and $\kappa_{\rm ctm}$ scales with p_v (which varies by a factor of 700). However, $\kappa_{\rm lines}$ also exhibits a temperature scaling, which we ignore and which accounts for much of the error in the slope of κ in Fig. A1a. At the same time, $\kappa_{\rm ctm}$ also exhibits a temperature scaling but with opposite sign, which *weakens* its Clausius–Clapeyron scaling [Eq. (A2)]. These opposing temperature scalings for $\kappa_{\rm lines}$ and $\kappa_{\rm ctm}$ modify our naive expectations, and seem to conspire to produce surprisingly similar overall logarithmic slopes. Whether or not this is a coincidence, or is related to the hypothesis that continuum absorption is simply due to far-wing line absorption (e.g., Ma et al. 2008), could be investigated further.

APPENDIX B

On the Emission Level Approximation and the Choice of $\tau_{\rm em}$

In sections 2 and 5 we made the "emission level" approximation that emission to space can be regarded as originating from a single level. We take this level to be the surface when

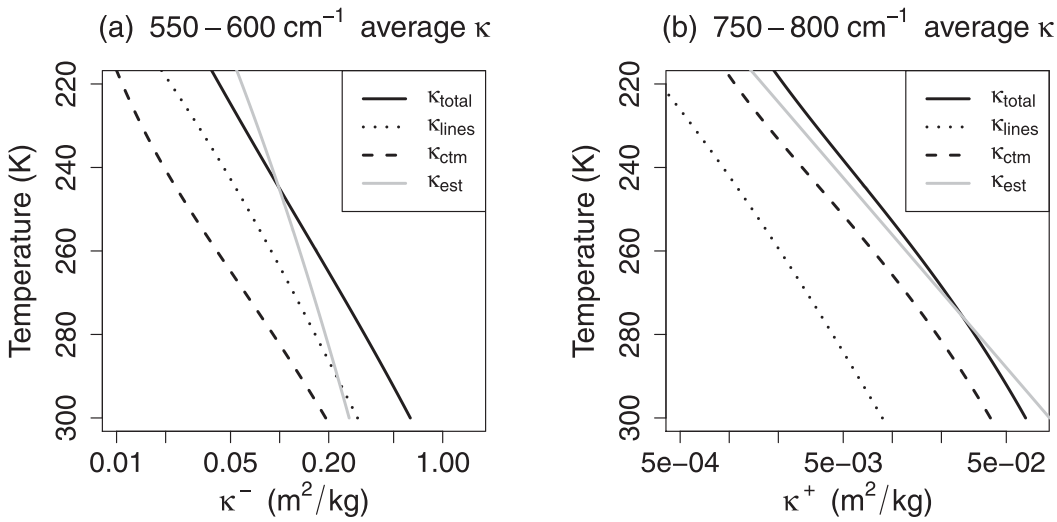

FIG. A1. Profiles of various contributions to spectrally averaged H_2O absorption coefficients in our BASE column for the wavenumber regions (a) 525–625 and (b) 725–825 cm^{-1}. The profiles of $\kappa_{\rm tot}$, $\kappa_{\rm lines}$, and $\kappa_{\rm ctm}$ are calculated with RFM, whereas $\kappa_{\rm est}$ is given by Eqs. (10) with $(\kappa^-_{\rm ref}, \kappa^+_{\rm ref})$ set to $(\kappa^-_{\rm tot}(T^-_{\rm ref}), \kappa^+_{\rm tot}(T^+_{\rm ref}))$, and where $(T^-_{\rm ref}, T^+_{\rm ref}) = (245, 275)$ K. The estimated profile κ^- is a poor approximation to $\kappa^-_{\rm tot}$, far from $T^-_{\rm ref}$ due to our neglect of temperature scaling of line absorption, but is acceptably close within 20 K or so of $T^-_{\rm ref}$. The horizontal axis in both panels is logarithmic, with the same geometric range (of 150) in each.

the atmosphere is sufficiently optically thin, and we set these levels as $\tau^{\rm CO_2}_{\rm em} = 0.5$ and $\tau^{\rm H_2O}_{\rm em} = 0.6$ when the surface optical depth is greater than those values. This appendix discusses this approximation, and justifies these choices of $\tau_{\rm em}$ for our applications. Other values of $\tau_{\rm em}$ may be required for other applications. Note also that the emission level we define here is distinct from the more general emission level defined in Dufresne et al. (2020); their emission level characterizes atmospheric emission even in the optically thin limit. Furthermore, our emission level $\tau_{\rm em}$ need not coincide with the maximum of the "weighting function" or the cooling-to-space profile, though these also occur at $\tau \sim O(1)$ (Jeevanjee and Fueglistaler 2020a).

It will be convenient to use the framework and notation of Jeevanjee and Fueglistaler (2020a), which considers a gray gas with idealized optical depth, temperature, and source function profiles

$$\tau = \tau_s\left(\frac{p}{p_s}\right)^{\beta}, \quad T = T_s\left(\frac{p}{p_s}\right)^{R_d\Gamma/g}, \quad B = B_s\left(\frac{T}{T_s}\right)^{\alpha},$$

where subscript s denotes the surface value of a quantity and B has units of W m^{-2}. These profiles combine to yield

$$B(\tau) = B_s\left(\frac{\tau}{\tau_s}\right)^{\gamma}, \quad \text{where} \tag{B1}$$

$$\gamma \equiv \frac{d\ln B}{d\ln\tau} = \alpha\frac{R_d\Gamma}{g}\frac{1}{\beta}. \tag{B2}$$

Now, the emission level (EL) approximation simply says that

$$\text{OLR} \approx \begin{cases} B_s & \text{if} \quad \tau_s < \tau_{\rm em} \\ B(\tau_{\rm em}) & \text{if} \quad \tau_s \geq \tau_{\rm em} \end{cases} \qquad \text{(EL approximation)} \tag{B3}$$

for some emission level optical depth $\tau_{\rm em}$, which may depend on the parameters introduced above. This $\tau_{\rm em}$ may be thought of as characterizing the transition between surface and atmospheric emission, or equivalently between optically thin and optically thick regimes. As such, we expect $\tau_{\rm em} \sim O(1)$ (Jeevanjee and Fueglistaler 2020b; Petty 2006; Wallace and Hobbs 2006), as we will indeed find below. Note that in terms of an effective emission temperature $T_{\rm em}$ which satisfies OLR $\approx B(T_{\rm em})$, the EL approximation can be rewritten as

$$T_{\rm em} = \min[T_s, T(\tau_{\rm em})], \tag{B4}$$

which is the form used in the main text [e.g., Eq. (8)].

To determine $\tau_{\rm em}$, we first analytically compute the OLR for our idealized gray gas,[B1] using Eq. (B1) and assuming $\tau_s \gg 1$:

$$\begin{aligned} \text{OLR} &= \int_0^{\infty} B_s(\tau/\tau_s)^{\gamma}e^{-\tau}\,d\tau \\ &= \frac{B_s}{\tau_s^{\gamma}}\tilde{\Gamma}(1+\gamma), \end{aligned} \tag{B5}$$

where $\tilde{\Gamma}(\gamma+1) \equiv \int_0^{\infty} x^{\gamma}e^{-x}\,dx$ denotes Euler's gamma function, and the tilde is introduced to distinguish it from the atmospheric lapse rate. We may then combine Eqs. (B1), (B3), and (B5) and solve for $\tau_{\rm em}$, obtaining

$$\tau_{\rm em} = [\tilde{\Gamma}(1+\gamma)]^{1/\gamma}. \tag{B6}$$

A plot of this curve is shown in Fig. B1a. To determine $\tau_{\rm em}$, then, we simply need appropriate values for γ for CO_2 and

[B1] We continue to employ a two-stream approximation and assume here that τ implicitly contains a diffusivity factor.

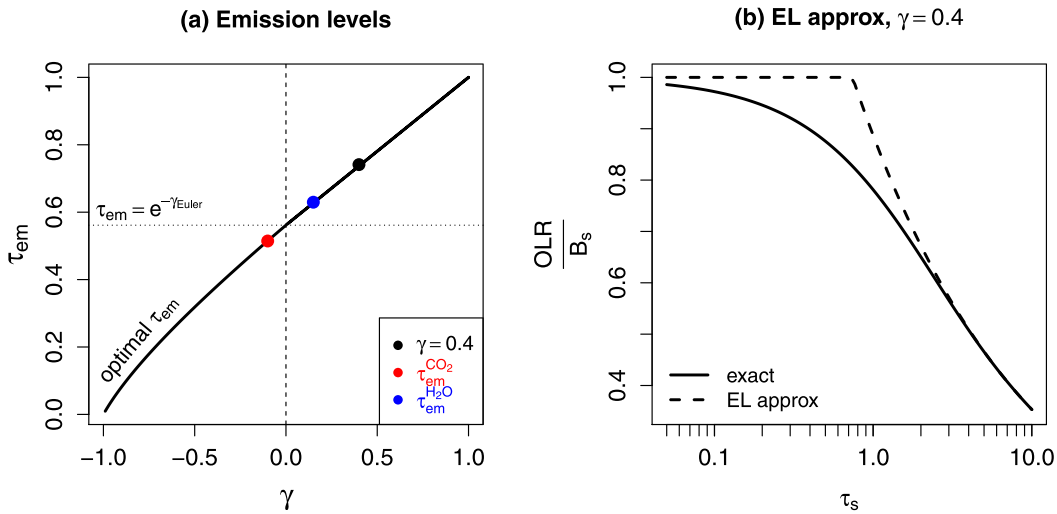

FIG. B1. (a) Plot of Eq. (B6) for emission levels $\tau_{\rm em}$ as a function of the parameter γ defined in (B2). At $\gamma = 0$, $\tau_{\rm em} = e^{-\gamma_{\rm Euler}} \approx 0.56$, close to our values for $\tau_{\rm em}^{\rm CO_2}$ and $\tau_{\rm em}^{\rm H_2O}$. (b) Plot of normalized exact OLR from Eq. (B7), as well as normalized OLR from the emission level approximation (B3) as a function of τ_s and with $\gamma = 0.4$ (black dot in left panel; see text for discussion of this value). The EL approximation is reasonable, even near $\tau_s = 1$, with maximum errors of roughly 15%.

H_2O emission. For CO_2, $\tau_{\rm em}$ only enters our theory quantitatively in determining $p_0(q)$ [Eq. (3)], which lies in the stratosphere where $\Gamma \approx -2\,{\rm K\,km^{-1}}$. Using this value for Γ and also setting $\beta = 2$ [Eq. (2)] and $\alpha = 4$ (Jeevanjee and Fueglistaler 2020a), Eq. (B2) then yields $\gamma^{\rm CO_2} = -0.1$. Plugging this into (B6) yields $\tau_{\rm em}^{\rm CO_2} \approx 0.5$ (Fig. B1a, red dot).

For H_2O, we are interested in tropospheric emission ($\Gamma \approx 7\,{\rm K\,km^{-1}}$) in the neighborhood of the CO_2 band ($\alpha = 4$). Jeevanjee and Fueglistaler (2020b) found $\beta = 5.5$ for line absorption,[B2] thus yielding $\gamma^{\rm H_2O} = 0.15$ and hence $\tau_{\rm em}^{\rm H_2O} = 0.6$ (Fig. B1a, blue dot).

With Eq. (B6) in hand, we may also explicitly evaluate the accuracy of the EL approximation (B3) across a range of τ_s values. To do this we need an exact expression for the OLR, generalizing (B5) and valid for all τ_s:

$$\begin{aligned} {\rm OLR} &= B_s e^{-\tau_s} + \int_0^{\tau_s} B_s (\tau/\tau_s)^{\gamma} e^{-\tau}\, d\tau \\ &= B_s e^{-\tau_s} + \frac{B_s}{\tau_s^{\gamma}} \tilde{\Gamma}(1+\gamma, \tau_s), \end{aligned} \tag{B7}$$

where $\tilde{\Gamma}(1+\gamma, \tau_s) \equiv \int_0^{\tau_s} x^{\gamma} e^{-x}\, dx$ is now the (lower) incomplete gamma function, which differs from Euler's gamma function only in the upper limit of the integral. We compare Eq. (B7) to the EL approximation (B3) in Fig. B1b. We choose $\gamma = 0.4$ (black dot in Fig. B1a), as it is appropriate for tropospheric CO_2 (Jeevanjee and Fueglistaler 2020a) and yields larger errors than the tropospheric H_2O value of $\gamma = 0.15$, allowing for a more conservative error assessment. Even with this conservative value of γ, the EL approximation is quite reasonable: errors never exceed 15% or so. For $\gamma = 0.15$, the errors do not exceed 7%. For greenhouses gases besides H_2O and CO_2, however, the value of γ may vary beyond the range considered here; see Jeevanjee and Fueglistaler (2020a) for further discussion.

Finally, we note that the γ parameter of Eq. (B2) was also found by Jeevanjee and Fueglistaler (2020a) to determine the validity of the cooling-to-space approximation, which holds when $\gamma \ll 1$. In this limit, we may Taylor-expand the $\tilde{\Gamma}$ function in (B6) and invoke the fact that $[d\tilde{\Gamma}(x)/dx]|_{x=1} = -\gamma_{\rm Euler}$, where $\gamma_{\rm Euler}$ is the Euler-Mascheroni constant (yet another gamma). A little calculation then shows that

$$\lim_{\gamma \to 0} \tau_{\rm em} = e^{-\gamma_{\rm Euler}} = 0.56. \tag{B8}$$

This gives a preferred value for $\tau_{\rm em}$ when $|\gamma| \ll 1$ (Fig. B1a, dotted horizontal line), and indeed this value is very close to both $\tau_{\rm em}^{\rm CO2}$ and $\tau_{\rm em}^{\rm H2O}$.

[B2] A β value appropriate for continuum absorption can be read off from Eq. (13) of Jeevanjee and Fueglistaler (2020b) by doubling the contribution from Clausius-Clapeyron scaling due to the quadratic dependence of continuum absorption on vapor pressure, which roughly doubles β to 10. This halves $\gamma^{\rm H2O}$ to 0.08, but yields negligible changes in $\tau_{\rm em}^{\rm H2O}$ (Fig. B1a).

REFERENCES

Butchart, N., and Coauthors, 2011: Multimodel climate and variability of the stratosphere. *J. Geophys. Res.*, **116**, D05102, https://doi.org/10.1029/2010JD014995.

Byrne, B., and C. Goldblatt, 2014: Radiative forcing at high concentrations of well-mixed greenhouse gases. *Geophys. Res. Lett.*, **41**, 152–160, https://doi.org/10.1002/2013GL058456.

Chung, E.-S., and B. J. Soden, 2015a: An assessment of direct radiative forcing, radiative adjustments, and radiative feedbacks in coupled ocean–atmosphere models. *J. Climate*, **28**, 4152–4170, https://doi.org/10.1175/JCLI-D-14-00436.1.

——, and ——, 2015b: An assessment of methods for computing radiative forcing in climate models. *Environ. Res. Lett.*, **10**, 74004, https://doi.org/10.1088/1748-9326/10/7/074004.

Clough, S. A., M. J. Iacono, and J. Moncet, 1992: Line-by-line calculations of atmospheric fluxes and cooling rates: Application to water vapor. *J. Geophys. Res.*, **97**, 15761, https://doi.org/10.1029/92JD01419.

Coakley, J. A., Jr., and P. Yang, 2014: *Atmospheric Radiation: A Primer with Illustrative Solutions*. Wiley, 256 pp.

Crisp, D., S. B. Fels, and M. D. Schwarzkopf, 1986: Approximate methods for finding CO_2 15-μm band transmission in planetary atmospheres. *J. Geophys. Res.*, **91**, 11851, https://doi.org/10.1029/JD091iD11p11851.

Curtis, A., and R. M. Goody, 1956: Thermal radiation in the upper atmosphere. *Proc. Roy. Soc. London*, **236A**, 193–206, https://doi.org/10.1098/rspa.1956.0128.

Donner, L. J., and Coauthors, 2011: The dynamical core, physical parameterizations, and basic simulation characteristics of the atmospheric component AM3 of the GFDL global coupled model CM3. *J. Climate*, **24**, 3484–3519, https://doi.org/10.1175/2011JCLI3955.1.

Dudhia, A., 2017: The Reference Forward Model (RFM). *J. Quant. Spectrosc. Radiat. Transfer*, **186**, 243–253, https://doi.org/10.1016/j.jqsrt.2016.06.018.

Dufresne, J. L., V. Eymet, C. Crevoisier, and J. Y. Grandpeix, 2020: Greenhouse effect: The relative contributions of emission height and total absorption. *J. Climate*, **33**, 3827–3844, https://doi.org/10.1175/JCLI-D-19-0193.1.

Feldl, N., and G. H. Roe, 2013: The nonlinear and nonlocal nature of climate feedbacks. *J. Climate*, **26**, 8289–8304, https://doi.org/10.1175/JCLI-D-12-00631.1.

Feldman, D. R., W. D. Collins, R. Pincus, X. Huang, and X. Chen, 2014: Far-infrared surface emissivity and climate. *Proc. Natl. Acad. Sci. USA*, **111**, 16 297–16 302, https://doi.org/10.1073/pnas.1413640111.

Fels, S. B., J. D. Mahlman, M. D. Schwarzkopf, and R. W. Sinclair, 1980: Stratospheric sensitivity to perturbations in ozone and carbon dioxide: Radiative and dynamical response. *J. Atmos. Sci.*, **37**, 2265–2297, https://doi.org/10.1175/1520-0469(1980)037<2265:SSTPIO>2.0.CO;2.

Flanner, M. G., X. Huang, X. Chen, and G. Krinner, 2018: Climate response to negative greenhouse gas radiative forcing in polar winter. *Geophys. Res. Lett.*, **45**, 1997–2004, https://doi.org/10.1002/2017GL076668.

Flato, G., and Coauthors, 2013: Evaluation of climate models. *Climate Change 2013: The Physical Science Basis*, T. F. Stocker et al., Eds., Cambridge University Press, 741–866.

Forster, P. M., and Coauthors, 2011: Evaluation of radiation scheme performance within chemistry climate models. *J. Geophys. Res.*, **116**, D10302, https://doi.org/10.1029/2010JD015361.

Freese, L. M., and T. W. Cronin, 2021: Antarctic radiative and temperature responses to a doubling of CO_2. *Geophys. Res. Lett.*, **48**, e2021GL093676, https://doi.org/10.1029/2021GL093676.

Govindasamy, B., and K. Caldeira, 2000: Geoengineering Earth's radiation balance to mitigate CO_2-induced climate change. *Geophys. Res. Lett.*, **27**, 2141–2144, https://doi.org/10.1029/1999GL006086.

Hansen, J., M. Sato, and R. Ruedy, 1997: Radiative forcing and climate response. *J. Geophys. Res.*, **102**, 6831–6864, https://doi.org/10.1029/96JD03436.

Hoffman, P. F., and Coauthors, 2017: Snowball Earth climate dynamics and Cryogenian geology-geobiology. *Sci. Adv.*, **3**, e1600983, https://doi.org/10.1126/sciadv.1600983.

Huang, Y., X. Tan, and Y. Xia, 2016: Inhomogeneous radiative forcing of homogeneous greenhouse gases. *J. Geophys. Res. Atmos.*, **121**, 2780–2789, https://doi.org/10.1002/2015JD024569.

Ingram, W. J., 2010: A very simple model for the water vapour feedback on climate change. *Quart. J. Roy. Meteor. Soc.*, **136**, 30–40, https://doi.org/10.1002/qj.546.

IPCC, 1994: Climate change 1994: Radiative forcing of climate change and an evaluation of the IPCC 1992 IS92 emission scenarios. J. T. Houghton et al., Eds., Cambridge University Press, 889 pp.

Jeevanjee, N., 2018: The physics of climate change: Simple models in climate science. https://arxiv.org/abs/1802.02695.

——, and D. M. Romps, 2018: Mean precipitation change from a deepening troposphere. *Proc. Natl. Acad. Sci. USA*, **115**, 11 465–11 470, https://doi.org/10.1073/pnas.1720683115.

——, and S. Fueglistaler, 2020a: On the cooling-to-space approximation. *J. Atmos. Sci.*, **77**, 465–478, https://doi.org/10.1175/JAS-D-18-0352.1.

——, and ——, 2020b: Simple spectral models for atmospheric radiative cooling. *J. Atmos. Sci.*, **77**, 479–497, https://doi.org/10.1175/JAS-D-18-0347.1.

——, D. D. B. Koll, and N. Lutsko, 2021: "Simpson's Law" and the spectral cancellation of climate feedbacks. *Geophys. Res. Lett.*, **48**, e2021GL093699, https://doi.org/10.1029/2021GL093699.

Kiehl, J. T., and B. P. Briegleb, 1993: The relative roles of sulfate aerosols and greenhouse gases. *Science*, **260**, 311–314, https://doi.org/10.1126/science.260.5106.311.

Koll, D. D. B., and T. W. Cronin, 2018: Earth's outgoing longwave radiation linear due to H_2O greenhouse effect. *Proc. Natl. Acad. Sci. USA*, **115**, 10 293–10 298, https://doi.org/10.1073/pnas.1809868115.

Ma, Q., R. H. Tipping, and C. Leforestier, 2008: Temperature dependences of mechanisms responsible for the water-vapor continuum absorption. I. Far wings of allowed lines. *J. Chem. Phys.*, **128**, 124313, https://doi.org/10.1063/1.2839604.

McKim, B., N. Jeevanjee, and G. K. Vallis, 2021: Joint dependence of longwave feedback on surface temperature and relative humidity. *Geophys. Res. Lett.*, **48**, e2021GL094074, https://doi.org/10.1029/2021GL094074.

Mlawer, E. J., V. H. Payne, J.-L. Moncet, J. S. Delamere, M. J. Alvarado, and D. C. Tobin, 2012: Development and recent evaluation of the MT_CKD model of continuum absorption. *Philos. Trans. Roy. Soc. London*, **A370**, 2520–2556, https://doi.org/10.1098/rsta.2011.0295.

Mlynczak, M. G., and Coauthors, 2010: Observations of infrared radiative cooling in the thermosphere on daily to multiyear timescales from the TIMED/SABER instrument. *J. Geophys. Res.*, **115**, A03309, https://doi.org/10.1029/2009JA014713.

——, and Coauthors, 2016: The spectroscopic foundation of radiative forcing of climate by carbon dioxide. *Geophys. Res. Lett.*, **43**, 5318–5325, https://doi.org/10.1002/2016GL068837.

Myhre, G., and F. Stordal, 1997: Role of spatial and temporal variations in the computation of radiative forcing and GWP. *J. Geophys. Res.*, **102**, 11 181–11 200, https://doi.org/10.1029/97JD00148.

——, E. J. Highwood, K. P. Shine, and F. Stordal, 1998: New estimates of radiative forcing due to well mixed greenhouse gases. *Geophys. Res. Lett.*, **25**, 2715–2718, https://doi.org/10.1029/98GL01908.

Nakajima, S., Y.-Y. Hayashi, and Y. Abe, 1992: A study on the "runaway greenhouse effect" with a one-dimensional radiative-convective equilibrium model. *J. Atmos. Sci.*, **49**, 2256–2266, https://doi.org/10.1175/1520-0469(1992)049<2256:ASOTGE>2.0.CO;2.

Oreopoulos, L., and Coauthors, 2012: The continual intercomparison of radiation codes: Results from phase I. *J. Geophys. Res.*, **117**, D06118, https://doi.org/10.1029/2011JD016821.

Paynter, D., and V. Ramaswamy, 2012: Variations in water vapor continuum radiative transfer with atmospheric conditions. *J. Geophys. Res.*, **117**, D16310, https://doi.org/10.1029/2012JD017504.

Petty, G. W., 2006: *A First Course in Atmospheric Radiation*. 2nd ed. Sundog Publishing, 472 pp.

Pierrehumbert, R. T., 1998: Lateral mixing as a source of subtropical water vapor. *Geophys. Res. Lett.*, **25**, 151–154, https://doi.org/10.1029/97GL03563.

——, 2004: High levels of atmospheric carbon dioxide necessary for the termination of global glaciation. *Nature*, **429**, 646–649, https://doi.org/10.1038/nature02640.

——, 2010: *Principles of Planetary Climate.* Cambridge University Press, 652 pp.

——, and R. Roca, 1998: Evidence for control of Atlantic subtropical humidity by large scale advection. *Geophys. Res. Lett.*, **25**, 4537–4540, https://doi.org/10.1029/1998GL900203.

Pincus, R., and Coauthors, 2015: Radiative flux and forcing parameterization error in aerosol-free clear skies. *Geophys. Res. Lett.*, **42**, 5485–5492, https://doi.org/10.1002/2015GL064291.

——, and Coauthors, 2020: Benchmark calculations of radiative forcing by greenhouse gases. *J. Geophys. Res. Atmos.*, **125**, e2020JD033483, https://doi.org/10.1029/2020JD033483.

Ramaswamy, V., and Coauthors, 2001: Radiative forcing of climate change. *Climate Change 2001: The Scientific Basis*. IPCC, 349–416 pp.

——., and Coauthors, 2019: Radiative forcing of climate: The historical evolution of the radiative forcing concept, the forcing agents and their quantification, and applications. *A Century of Progress in Atmospheric and Related Sciences: Celebrating the American Meteorological Society Centennial*, *Meteor. Monogr.*, **59**, 14.1–14.101, https://doi.org/10.1175/AMSMONOGRAPHS-D-19-0001.1.

Richardson, T. B., and Coauthors, 2019: Efficacy of climate forcings in PDRMIP models. *J. Geophys. Res. Atmos.*, **124**, 12 824–12 844, https://doi.org/10.1029/2019JD030581.

Rind, D., and A. Lacis, 1993: The role of the stratosphere in climate change. *Surv. Geophys.*, **14**, 133–165, https://doi.org/10.1007/BF02179221.

Schmithüsen, H., J. Notholt, G. König-Langlo, P. Lemke, and T. Jung, 2015: How increasing CO_2 leads to an increased negative greenhouse effect in Antarctica. *Geophys. Res. Lett.*, **42**, 10 422–10 428, https://doi.org/10.1002/2015GL066749.

Seeley, J. T., 2018: Convection, radiation, and climate: Fundamental mechanisms and impacts of a changing atmosphere. Ph.D. dissertation, University of California, 137 pp., https://digitalassets.lib.berkeley.edu/etd/ucb/text/Seeley_berkeley_0028E_18385.pdf.

Sejas, S. A., M. Cai, G. Liu, P. C. Taylor, and K. Tung, 2016: A Lagrangian view of longwave radiative fluxes for understanding the direct heating response to a CO_2 increase. *J. Geophys. Res. Atmos.*, **121**, 6191–6214, https://doi.org/10.1002/2015JD024738.

——, P. C. Taylor, and M. Cai, 2018: Unmasking the negative greenhouse effect over the Antarctic Plateau. *npj Climate Atmos. Sci.*, **1** (17), https://doi.org/10.1038/s41612-018-0031-y.

Sherwood, S. C., S. Bony, O. Boucher, C. S. Bretherton, P. M. Forster, J. M. Gregory, and B. Stevens, 2015: Adjustments in the forcing-feedback framework for understanding climate change. *Bull. Amer. Meteor. Soc.*, **96**, 217–228, https://doi.org/10.1175/BAMS-D-13-00167.1.

Shine, K. P., and P. M. F. Forster, 1999: The effect of human activity on radiative forcing of climate change: A review of recent developments. *Global Planet. Change*, **20**, 205–225, https://doi.org/10.1016/S0921-8181(99)00017-X.

——, I. V. Ptashnik, and G. Rädel, 2012: The water vapour continuum: Brief history and recent developments. *Surv. Geophys.*, **33**, 535–555, https://doi.org/10.1007/s10712-011-9170-y.

Simpson, G., 1928: Some studies in terrestrial radiation. *Memoirs Roy. Meteor. Soc.*, **2**, 69–95.

Smith, K. L., G. Chiodo, M. Previdi, and L. M. Polvani, 2018: No surface cooling over Antarctica from the negative greenhouse effect associated with instantaneous quadrupling of CO_2 concentrations. *J. Climate*, **31**, 317–323, https://doi.org/10.1175/JCLI-D-17-0418.1.

Soden, B. J., W. D. Collins, and D. R. Feldman, 2018: Reducing uncertainties in climate models. *Science*, **361**, 326–327, https://doi.org/10.1126/science.aau1864.

Strow, L. L., D. C. Tobin, and S. E. Hannon, 1994: A compilation of first-order line-mixing coefficients for CO_2 Q-branches. *J. Quant. Spectrosc. Radiat. Transfer*, **52**, 281–294, https://doi.org/10.1016/0022-4073(94)90158-9.

Wallace, J. M., and P. V. Hobbs, 2006: *Atmospheric Science: An Introductory Survey.* Academic Press, 504 pp.

Wang, Y., and Y. Huang, 2020: Understanding the atmospheric temperature adjustment to CO_2 perturbation at the process level. *J. Climate*, **33**, 787–803, https://doi.org/10.1175/JCLI-D-19-0032.1.

Wilson, D. J., and J. Gea-Banacloche, 2012: Simple model to estimate the contribution of atmospheric CO_2 to the Earth's greenhouse effect. *Amer. J. Phys.*, **80**, 306–315, https://doi.org/10.1119/1.3681188.

Zhang, M., and Y. Huang, 2014: Radiative forcing of quadrupling CO_2. *J. Climate*, **27**, 2496–2508, https://doi.org/10.1175/JCLI-D-13-00535.1.

Zhao, M., and Coauthors, 2018: The GFDL global atmosphere and land model AM4.0/LM4.0: 2. Model description, sensitivity studies, and tuning strategies. *J. Adv. Model. Earth Syst.*, **10**, 735–769, https://doi.org/10.1002/2017MS001209.

Zhong, W., and J. D. Haigh, 2013: The greenhouse effect and carbon dioxide. *Weather*, **68**, 100–105, https://doi.org/10.1002/wea.2072.